

NASA Contractor Report 180846

LEWIS GRANT

IN-02

119483

91P

A Flow Visualization Study of the Leading Edge Separation Bubble on a NACA 0012 Airfoil With Simulated Glaze Ice

(NASA-CR-180846) A FLOW VISUALIZATION STUDY
OF THE LEADING EDGE SEPARATION BUBBLE ON A
NACA 0012 AIRFOIL WITH SIMULATED GLAZE ICE
Final Report M.S. Thesis (Ohio State Univ.)
91 p

N88-14966

Unclas
0119483

CSCL 01A G3/02

Abdollah Khodadoust
The Ohio State University
Columbus, Ohio

January 1988

Prepared for
Lewis Research Center
Under Grant NAG3-28



National Aeronautics and
Space Administration

ACKNOWLEDGEMENTS

The author would like to thank his advisor, Dr. Michael Bragg, for his guidance and support throughout this effort. Gratitude is also expressed to the entire staff of the Ohio State Aeronautical and Astronautical Research Laboratory who helped in organizing and conducting the experiments.

This work was funded in part by the National Aeronautics and Space Administration Lewis Research Center under grant number NAG 3-28.

TABLE OF CONTENTS

ACKNOWLEDGEMENTS

i

CHAPTER

I.	INTRODUCTION	1
II.	SURVEY OF LITERATURE	3
	Laminar Separation Bubbles	
	Airfoil Icing	
III.	EXPERIMENTAL EQUIPMENT AND TECHNIQUE	9
	Wind Tunnel and Model	
	Equipment and Technique	
	Tuft Flow Study	
	Oil Flow Study	
	Smoke Flow Study	
	Liquid Crystal Flow Study	
IV.	RESULTS AND DISCUSSION	18
	Analysis of Photographs	
	Tuft Flow Visualization	
	Splitter Plate Flow Visualization	

iii

PRECEDING PAGE BLANK NOT FILMED

PAGE ii INTENTIONALLY BLANK

Oil Flow Visualization
Smoke Flow Visualization
Liquid Crystal Flow Visualization

Comparison With Other Data

Tuft Flow Visualization
Splitter Plate Flow Visualization
Oil Flow Visualization
Comparison of Experimental Data

V. CONCLUSIONS AND RECOMMENDATIONS	34
LIST OF REFERENCES	37
FIGURES	40
TABLES	71
APPENDIX	81

I. Introduction

The accretion of structural ice on aircraft in flight causes a loss in operational efficiency and, more importantly, a reduced safety margin. While de-icing and anti-icing systems are available and work well in many applications, they have a high initial cost, add weight to the aircraft, and are expensive to maintain. Therefore many airfoil surfaces on aircraft are unprotected and designers would like to protect as few surfaces as possible. Therefore it is important to understand the accretion of ice on unprotected airfoils and the resultant aerodynamic effects [1].

The effects of ice growth on the performance of an aircraft are primarily felt through aerodynamic penalties: a drastic reduction in maximum lift coefficient and stall angle and an increase in drag. The two classes of ice accretions known as rime and glaze, are formed under different flight conditions. Rime ice is formed at low temperatures and low velocities. The droplets freeze on impact and usually are found in flight through clouds with low liquid water content. Figure 1 shows an example of a rime ice accretion with its characteristic streamlined leading edge growth.

Glaze ice, on the other hand, is formed at temperatures near the freezing mark and higher velocities, and provides the largest aerodynamic penalties. In this type of ice growth, rather than

freezing on impact, the water droplets run back on the surface before freezing. The resulting shape with the characteristic horns is shown in figure 1. This type of ice formation on the airfoil leading edge is the subject of this paper.

Glaze ice formations on the airfoil leading edge cause a separation bubble to form aft of the ice horns, both on the upper and lower surface. This separation causes a large penalty in drag and a significant reduction in the maximum lift coefficient. The presence of this separation zone is well known and several researchers [1-9] have studied the flow about the leading edge of airfoils with this type of ice formation.

The study described in this paper applies current flow visualization techniques to help understand the flow field about an airfoil with glaze ice. These results are compared to the computational results and other experiments.

II. Survey of Literature

The study of leading edge separation bubble phenomenon as a result of airfoil icing can be historically traced back to two separate areas of aerodynamic research: leading edge separation bubbles, and airfoil icing. Early icing research was primarily involved in designing and testing ice protection systems. Although some aerodynamic measurements were made, no flow field details were measured. In the late 1970's, further research in airfoil icing required a better physical understanding of the separation bubble due to the ice shape. At that point, researchers began investigating the leading edge separation bubble and its relation to the early separation of the flow from the airfoil. In the following sections, a brief historical review of the literature on separation bubbles, and then airfoil aerodynamic performance in icing, is given.

Laminar Separation Bubbles

Much of early work on airfoils focused on bubbles that formed on the leading edge (short bubbles) as a result of an increase in angle of attack, and bubbles formed in the mid chord region (long bubbles). Lacking

the currently available computational power, researchers directed their efforts towards formulating empirical models of bubble growth and bursting phenomenon. In 1959, Horton [10] used a simple bubble model along with an approximate method to calculate the momentum thickness growth over the separation bubble, to devise a method to predict bubble growth, length, and height.

In 1966 Gaster [11], reflecting on the results of his studies on the separation bubble over the nose of a thin airfoil, pointed out that there is a physical limitation in the amount of pressure recovery possible in the shear layer. The bubble bursts when the limit is exceeded; as a result, a long bubble or a free shear layer may be created which in turn, causes an increase in drag and an undesirable change in pitching moment along with an appreciable fall in lift (thin airfoil nose stall). It is a phenomenon that can readily be seen in iced airfoils at much lower angles of attack.

In 1976 Crimi and Reeves [12] studied leading edge laminar separation bubbles and developed a scheme for predicting the onset of transition in the laminar shear layer. By the mid 1970's, some researchers began numerical investigation of separation bubbles. In 1974, Carter [13] investigated numerical solutions of laminar, incompressible boundary layer equations for flows with separation and reattachment. He used a stream function/vorticity formulation for the boundary-layer

equations. Solution of the resulting finite-difference equations, were obtained by a successive column iteration scheme. In 1975, Briley and McDonald [14] utilized the finite-difference solutions to the time dependent boundary-layer equations for the flow in the immediate vicinity of the bubble to carry out a detailed numerical study of thin incompressible separation bubbles on a NACA 66-018 airfoil at zero incidence and chord Reynolds numbers of 2.0×10^6 and 1.7×10^6 .

Currently, a majority of the research effort is focused on numerical investigation of the Navier-Stokes equations; and with the rapid progress in information processing speed in mind, the author has little doubt that further computational research in the area will be directed toward numerical investigation of existing equations.

Airfoil Icing

Initial investigations into icing were concerned with de-icing [15]. One of the first efforts involved the development of inflatable de-icing boots by B. F. Goodrich in the 1930's. While this concept is still in wide use, it poses major problems such as increased aircraft weight, lowered operational efficiency and higher maintenance cost. Consequently, attention has gradually shifted to the study of new ice protection concepts and the more fundamental areas of ice accretion

and aerodynamic penalties.

The first major investigation of icing characteristics and aerodynamic penalties associated with icing phenomena were performed by the NACA in the 1950's[2]. Experimental information was gathered for the NACA 65A004, 63A009, 0011, 65-212 and 63015 airfoils. In the 60's, Vernon Gray [2,3] drew correlations between estimating the size and type of ice formations as a result of any specific icing encounter. Gray developed empirical equations relating known icing conditions to the change in drag coefficient. However, no correlation between the type and size of leading edge separation bubble was drawn. Laschka and Jesse [16] made observations based on investigations made in the Lewis Icing Tunnel. They noted that many different ice shapes will be obtained with the variation of angle of attack. They also observed that the ice height is approximately proportional to the icing time (t), while impingement limits are time independent.

Since the late 1970's, experimental icing research on airfoil aerodynamics has increased with the works of Bragg, Shaw, Gregorek, Lee and others. Shaw [5] and Bragg et. al. [1,6,7] have continued experimental investigation into the 80's. By 1985, significant effort went into defining the region behind the leading edge ice formations. The recent focus of attention has been centered on glaze ice, which, between the two types

of ice formation (glaze and rime), causes the most severe aerodynamic penalties. Bragg and Coirier [7,8] measured the flow field in the vicinity of a NACA 0012 airfoil with a 5 minute glaze ice simulation. They documented the coefficients of lift and moment along with pressure and velocity distributions for the above model. For the recent studies, the NACA 0012 with the 5 minute simulated glaze ice model has become the standard model for icing research. In 1986, Bragg [9] published a comprehensive survey of all flow field measurements taken about the described model. Flow visualization data reported by Bragg gave some of the first information on the glaze ice separation bubble geometry.

Recently, researchers have been able to apply computational means to the problem of flow over airfoil with simulated ice. Cebeci [17] used a modified version of his interactive boundary layer technique to predict the aerodynamic characteristics of an airfoil with leading edge ice accretion. His results include values for coefficients of lift, drag, and skin friction as well as boundary layer thickness for various angles of attack. Potapczuk [18] used a parabolized Navier-Stokes model to make similar calculations. His calculations report coefficients of lift, drag and pressure along with velocity profiles at various chord locations. His code suggests the presence of a secondary separation bubble, located on the upper surface ice horn, inside a

bigger separation bubble. Experimental evidence verifying this type of bubble structure has not yet been obtained. Tang and Sankar [19] have applied another Navier-Stokes model to the same problem. The results of these calculations are very promising but more experimental data are needed to further develop these methods.

The study reported in this paper is part of a continued effort in aircraft icing research and a step toward validation of computational results and also other experimentally obtained results. By utilizing various flow visualization techniques, it is hoped that more physical information about the separation bubble geometry will be obtained, and combined with experimental data of Bragg, will verify the size of the separation bubble.

III. Experimental Apparatus and Technique

Wind Tunnel and Model

These tests were conducted in the Ohio State University's subsonic wind tunnel located at the Aeronautical and Astronautical Research Laboratory. The tunnel is of conventional design with approximately a three-by-five foot test section, eight feet in length. The tunnel operates at speeds from zero to 220 feet per second at Reynolds number up to 1.3×10^6 per foot. The tunnel is of open return type and uses four turbulence screens and honeycomb in the settling chamber to reduce the tunnel turbulence. For this series of tests, the tunnel was equipped with a motor driven angle of attack changer. The test section floor was painted flat black to aid with the background-foreground contrast while conducting smoke flow and oil flow studies. The tunnel will accommodate airfoils mounted vertically in the test section or three dimensional models, strut mounted using an internal strain gauge balance. Tunnel speed, Reynolds number and Mach number are measured through facility transducers.

A NACA 0012 model was used for this test. The model was made of a section of a UH1H helicopter rotor blade and was 21 inches in chord and had a span of 39

inches. The model was mounted vertically in the tunnel providing a tunnel height to chord ratio of 2.62. A wooden simulated ice shape was used with the model which was constructed to approximate an actual measured ice accretion. The ice was accreted in the NASA Lewis Research Center's Icing Research Tunnel on a NACA 0012 airfoil, also of 21 inch chord. In figure 2, the measured ice shape, as recorded from an actual tracing, is compared to the one used in this test.

For flow visualization purposes, the entire model with the simulated ice shape was painted glossy black. Since the model had twist, all data were taken and the angle of attack was reported on the model center line. The NACA 0012 airfoil coordinates clean (i.e. no ice shape attached) are given in table 1. The coordinates for the airfoil plus the ice model are given in table 2. In the following section, a description of material and equipment used in conducting and recording various types of flow visualization is given.

Equipment and Technique

Various methods of flow visualization were used in this study. Lighting for this experiment was accomplished by a series of high intensity 500 watt 3200 degrees Kelvin light bulbs. Depending on the amount of lighting needed and the time of day or night the experiment was conducted, one to four of these lights

were used. Figure 3 shows the optical arrangements used for the tests. Flow visualization results were recorded on both 1/2 inch VHS video tape using a RCA video recorder model CLC021 7-10 Lux Autofocus and 35 mm 160 ASA tungsten slide film using a Pentax K1000 camera with 50mm f:2.0 lense.

Tuft Flow Study: Tufts have the advantage that they respond to unsteady characteristics of the flow. Flow visualization using the method of surface tufts was accomplished by placing strips of tufts on both upper and lower surfaces of the test model. Tufts were placed in a more dense arrangement up to 15 percent chord, in order to get a more accurate reading of flow detachment and reversal. The problem of tuft interference with the flow was minimized by using dyed strands of 2mm diameter nylon monofilaments. In the denser region, 1/2 inch and one inch long tufts were used to avoid interference and on the rest of the airfoil surface, two inch long tufts were used. A small loop of thread was run through the tuft, and the thread was taped to the model to ensure free movement of the tuft. Tufts were taped to the model surface using cellophane tape at two inch intervals side by side. The photographic plate in figure 4 shows the arrangement of tufts for the upper surface of the test model. The tunnel was operated at 85 feet per second for this series of tests. The model was then set at angle of attack of -6 through +6 in 1

degree increments. The resulting tuft motion was then recorded using still photographs and VHS video tape.

Oil Flow Study: A 3:1 ratio of linseed oil and oil based artist's paint were used to make the mixture easier to apply and to reduce the paint viscosity. This series of tests were conducted in two stages. In the first stage, the mixture was applied in a thin coat to the entire upper and lower surfaces of the test model. The tunnel was then brought up to speed and oil mixture was allowed to deform under shear stress. Shear stress patterns in the oil mixture were recorded on 35 mm slides and 1/2 inch VHS video after the tunnel was brought to rest.

In the second stage, splitter plates were used on both surfaces. The splitter plates were constructed of two millimeter thick aluminum sheet, extending to 50 percent chord on the upper and the lower surfaces. A schematic of the splitter plate position and size is given in figure 5. The splitter plates were mounted on the airfoil surface such that they were flush with the iced model's leading edge. The two dimensionality of the flow over the splitter plates was insured by aligning the splitter plates parallel to the free stream flow. In this stage of tests, oil droplets were first placed on the splitter plate in a random fashion. Later, the entire splitter plates' surface was covered with a thin coating of the mixture. Two color pigments

(white and red) were used initially. However the contrasting colors proved to be of little use in visualizing the bubble contour; therefore, the white paint was used in all later tests and recordings. Similar to the method in the first stage, the tunnel was first brought up to speed and after the oil mixture was deformed under shear, the tunnel was shut down. Oil traces were recorded on both 35 mm slide film and 1/2 inch VHS video tape. Several different optical arrangements were tried. Lighting from the test section ceiling and sides proved the most useful in highlighting the results. In all cases, the tunnel was run at 180 feet per second and the test model was set at an angle of attack of -6 through +6 in 1 degree increments.

Smoke Flow Study: In the series of tests involving smoke flow visualization, Titanium Tetrachloride was considered initially. The choice was based on the property that this chemical will react with the moisture content of air to produce a very dense white smoke (TiO_2 particles) [20]. Experiments conducted by Bragg [8,9] suggested the presence of the separation bubble over the second pressure tap ($X/C = 0.02$) for all angles of attack tested. The idea was to insert the chemical in the pressure tube leading to the second pressure tap located at 2 percent of the chord on the airfoil. The chemical would then be released to seed the separation bubble with Titanium Oxide particles. This procedure

would eliminate the use of a smoke rake or smoke wand upstream of the test model, thereby eliminating the chance of flow contamination with the presence of a smoke rake or wand. In Figure 6 the Titanium Tetrachloride test rig is shown. Theoretically, the idea seemed very feasible; however, in practice this chemical proved to be very hard to work with. There was a problem associated with the rapid buildup of Titanium Oxide residue on the model surface. The buildup happened at such a fast rate that it altered the nature of the flow in the vicinity of the bubble. The difficulties involved in handling Titanium Tetrachloride and the difficulty in getting the equipment to work properly, were enough reasons to explore other alternatives.

A variety of materials and chemical compounds have been used in the past to produce dense smoke suitable for flow visualization. Table 3 gives a list of some of the most commonly used substances along with their physical characteristics [21]. Traditionally, Kerosene smoke has proven to be quite a useful tool in flow visualization. Therefore attention was turned to building a Kerosene smoke generator capable of an output large enough to give quantitative information about the separation bubble. Figure 7 shows a detailed plan of the kerosene smoke generator built. The smoke generator is similar in design to that of Mueller's [22]. It consists of three electrical strip heaters that are

contained in a closed chamber. Droplets of kerosene are passed through three separate nozzles for each strip heater. Having separate access to electricity, each strip heater can be turned on and off independent of the other two. When hot, the strip heaters cause the kerosene to evaporate and produce a dense white smoke. Kerosene odor was overcome by using odorless kerosene. The extra, unevaporated kerosene rolls off the strip heaters and collects at the bottom of the chamber for later collection. This setup coupled with an electric thermostat connected to the strip heaters, controlled the temperature of the strip heaters.

The chamber is then pressurized by a Nitrogen tank which also cools the smoke down and minimizes the possibility of combustion. The pressurized smoke was then diverted into a tube leading to a 1/4 inch diameter smoke wand which was placed in the flow upstream of the test model. At this point, the idea of routing the smoke through pressure taps into the separation bubble became less of a reality. Earlier tests with Titanium Tetrachloride showed the amount of smoke injected into the mainstream from the pressure taps was not adequate to give a visible description of the separation bubble geometry. Several generators of the same design would lead to a sizeable amount of smoke output. However, an array of these units would be very costly; therefore, instead of the smoke rake design, the smoke wand was

used.

For better observation of the smoke flow pattern, the tests were conducted at night. A light sheet was constructed from an aluminum molding which formed a 1/4 inch wide by 21 inch long and three inch deep slit. Light produced from four high intensity 500 watt light bulbs passed through this slit to produce a one inch thick light sheet in the tunnel test section. In another series of tests involving smoke flow studies, the tunnel was operated with the light source being only that of a strobe light capable of generating frequencies ranging from 110 to 150,000 cycles per minute. Strobe light frequency was then altered at various stages of the test in order to freeze the bubble frequency.

Liquid Crystal Flow Study: Liquid crystals are a state of matter between solid and liquid [23], in which the molecules are elongated in one direction. Liquid crystals scatter light in accordance with the change in their helical structures' pitch length. Thus, when subjected to certain physical influences, the helix pitch length changes and the wavelength of reflected light changes accordingly [24]. Although discovered in 1888, liquid crystals have been applied in aerodynamic testing only since the early 1960's. While much is known about liquid crystals as thermal indicators, little information exists about their use for quantitative shear stress analysis.

For these tests, cholesteric liquid crystals were used. The liquid crystals were mixed with liquid freon in a 1:8 solution and then were applied onto the model surface using a spray gun with 25 psi of air pressure.

The series of experiments conducted with the liquid crystal solution proved to be harder than initially expected. Although this material holds great promise as a tool for aerodynamic shear stress analysis, it did not live up to it's potential in these experiments. The solution, however, did respond to the surface shear stress. Certain color changes in the liquid crystals, associated with the change in shear stress due to separation and reattachment of the flow, were observed on the surface of the airfoil. Figure 8 shows a photograph taken while conducting tests using liquid crystals. On the photograph, the region of reattachment has been marked by an arrow. The liquid crystal solution did not provide similar results for all of the angles under study. More detailed knowledge of the liquid crystals' physical characteristics is needed before successful experiments can be conducted with this substance.

IV. Results and Discussion

The results of this experimental study are presented in two parts. In the first part, results which were recorded on photographs are analyzed. Features such as separation, reattachment, surface shear, and separation streamlines are discussed. In the second part, the data reduced from oil, tuft, and splitter plate flow visualization photographs are compared to the data from references 9 and 17.

Analysis of Photographs

A diagram of a typical flow pattern observed with a separation bubble is shown in Figure 9. As the flow passes over the ice horn on the leading edge, it meets a region of severe adverse pressure gradient. As a result, the flow loses momentum and the laminar boundary layer separates from the surface which leads to the region of recirculation. Transition to turbulent flow occurs in the separated shear layer shortly before reattachment. Turbulent mixing allows the separated boundary layer to gain enough energy to reattach. The separation streamline is defined as that streamline which isolates the mass of fluid in the bubble from the mass of the outside fluid. In figure 9, this streamline

is identified as the first streamline which reattaches after separation. The area below the separation line is known as the recirculating region or the separation bubble.

The general pattern of behavior mentioned above has been observed through different flow visualization methods. Each method has highlighted a certain aspect of the phenomena under study.

Tuft Flow Visualization: Data recorded on slide photographs were used for analysis in this section. Figure 10 shows the separation bubble through the method of tuft flow visualization. While the slide photographs reveal an instantaneous picture of the flow over the airfoil, the tuft flow visualization recorded on the video brings a "real time" image of the tuft motion into perspective. This is particularly useful when the airfoil angle of attack is set close to the angle beyond which the flow fails to reattach.

From the photographic slides, the length of the model was measured. The ratio of this measured length to the actual length of the model (21 inches) provided a length scale from which the reattachment points were accurately determined. The accuracy for calculation of the reattachment lines is on the order of half of the length of a tuft strand. In figure 11 the calculated position of the reattachment line along with the error

margin of that calculation are shown. In regions of the airfoil surface where the flow is attached, tufts are seen pointing in the direction of the model trailing edge (direction of flow) with very little flutter, while in the region of separated flow, tufts are seen to be pointing in different directions. Data reduced from flow visualization using the method of tufts is presented in table 4.

For the upper surface, the reattachment point is seen to progress towards the trailing edge; starting at 7 percent chord for zero degrees angle of attack and moving to 24 percent chord for 5 degrees angle of attack. At the instance the photograph was recorded, the reattachment point for 6 degrees was noted at 33 percent chord location. This data point could be highly inaccurate due to the very unsteady flow at this angle. This is the angle beyond which the flow fails to reattach. Photographic plates taken at 7 degrees show a completely stalled upper surface.

For the lower surface, the reattachment point was seen to move forward towards the leading edge for increasing positive values of angle of attack while for negative values, the reattachment point moved towards the trailing edge. The shortest reattachment distance measured was 10 percent chord at 5 degrees angle of attack and the longest one was 35 percent at -5 degrees angle of attack. At -6 degrees the flow separates from

the lower surface. Photographs taken at -6 degrees for the lower surface show a completely stalled wing.

Splitter Plate Flow Visualization: Figure 12 shows the separation bubble through the splitter plate flow visualization. Before the flow visualization tests using the method of splitter plate started, the NACA 0012 model was marked at ten percent chord intervals from the leading edge to the trailing edge. These marks later helped determine the reattachment point and the bubble shape. The oil flow pattern on the splitter plate was used to determine the location of the reattachment line. Separation streamline information can be obtained from the slide photographs; however, due to the restraint imposed by the path of observation, the separation bubble could not be sized accurately.

The oil flow pattern on the splitter plates located on both upper and lower surfaces of a NACA 0012 airfoil section is shown in plates of figure 12. The two dimensionality of the flow on the splitter plate can be checked by noting the nearly parallel streamlines shown on the oil traces for the outside flow.

Reattachment points observed from the splitter plate studies are listed in table 5. Reattachment lines were determined by correlating their location between the 10 percent chord interval markings. In plates of figure 12, the recirculating region behind the ice shape

has been circled for better identification. On the upper surface, this region is found to be quite small and very well defined at lower angles of attack. As the angle of attack is increased, this region grows in size and gradually loses its sharp definition on the splitter plate.

For the upper surface, only 5 data points were obtained. Although care was taken to ensure that the flow was two dimensional, the splitter plate interference could have been a possible factor, along with the unsteady bubble, in leading to an oil flow pattern which was not clearly visible.

The longest reattachment distance measured was 22 percent chord at 5 degrees angle of attack and the shortest reattachment distance measured was 4 percent chord at -2 degrees angle of attack on the upper surface. For the lower surface, all reattachment points from -4 degrees to +6 degrees were recorded. At -4 degrees the longest reattachment distance was recorded at 34 percent chord. Photographs for the -5 degrees case show an undefined oil flow pattern, which is indicative of a completely separated flow. The shortest reattachment distance for the lower surface was 9 percent chord at 5 degrees angle of attack.

Oil Flow Visualization: Figure 13 shows the separation bubble through oil flow visualization. Flow

visualization data for the method of surface oil flow were recorded on both photographic slides and video. However, only the results recorded on the photographic slides are presented for comparison with other data. The surface oil flow data recorded on video is particularly useful when it is desired to see the rapid formation of an oil flow pattern due to surface shear stress. In the photographic slides the final pattern of the shear stress is recorded. The boundary of the bubble along the chord is given as the line beyond which oil traces are sheared in the direction of the outside flow. The reattachment region is marked with an arrow in figure 13. The region of reattachment in this study appears as a band of low oil accumulation in the spanwise direction on the airfoil. The arrows on plates of figure 13 indicate where the general area is. Due to the unsteady nature of the bubble, this reattachment line does not appear as a line of solid oil texture. It, however, shows as a line which gradually appears and finalizes as a band of solid texture. In figure 13, the estimated error bound for that case are also shown.

It was noticed in this series of tests, that this band tends to be very wide which in turn decreases the accuracy of determining the reattachment line position. In general through trial and error and comparison with other data, it was found that the reattachment line is usually located aft of the region of low shear and

before the region of high shear. This area of high shear is indicated by bands of oil mixture usually streaking towards the trailing edge at lower angles of attack for both upper and lower surfaces.

Similar to the method in the tuft flow studies, the length of the model was measured. The ratio of this measured length to the actual length of the model provided a length scale from which the reattachment points were determined. Results of the oil flow visualization studies are given in table 8.

Also through trial and error, it was discovered that by varying the ratio of the oil mixture used for surface oil flow studies, the mixture could be made to highlight the surface shear pattern or ,if desired, the flow direction pattern could be highlighted. The surface shear pattern is highlighted in the top plate of figure 13 while in the bottom plate of figure 13 the flow direction lines are clearly emphasized by streaks of oil running back towards the trailing edge.

The shortest reattachment distance measured was 5.7 percent chord at -6 degrees angle of attack on the upper surface and 12 percent chord at 5 degrees angle of attack on the lower surface. The longest reattachment distance measured was 36.4 percent chord at 6 degrees on the upper surface and 45 percent chord at -6 degrees on the lower surface.

Smoke Flow Visualization: Results obtained from flow visualization with kerosene smoke were mainly qualitative. The lack of a sufficient volume of smoke prevented a full investigation of the leading edge separation bubble. The photographs and, especially, the video taken from the separation bubble while it was visualized with the smoke tube revealed very good qualitative information about the nature of the bubble.

Plates in figure 14 show a qualitative size of the leading edge separation bubble. The bubble is outlined with the aid of one smoke tube. For negative angles of attack, the bubble has a minimal effect on the local pressure coefficients on the upper surface while at positive angles, the outline of the bubble is quite obtrusive and affects the entire flow field.

Liquid Crystal Flow Visualization: Figure 8 shows an example of the results of liquid crystal flow visualization study. Although more information about liquid crystals and their properties are needed before they can be used effectively, the tests involving the use of liquid crystals showed what appears to be the reattachment line. Liquid crystals respond to change in surface shear by a color change and remain colorless when no shear is present. Arrows in figure 8 mark the region where the location of reattachment line is thought to be.

Comparison with Other Data

In the following sub-sections, data from oil flow, tuft flow, and splitter plate flow visualization techniques are compared to data of references 9 and 17. Due to the qualitative nature of the smoke flow and the liquid crystal flow visualization data, the results obtained by using these methods were not reduced into the form of reattachment lines.

As a baseline for comparison, the experimental data of references 9 and 25 and the computational data of reference 17 will be used. Published in January of 1987, data presented in ref 25 were the most up-to-date and recent information at the time of this writing. Bragg and Spring studied the effect of a simulated glaze ice accretion on the aerodynamic performance of a NACA 0012 airfoil. They used a split film probe to measure the velocity in the upper and lower surface separation bubbles.

However, the data of reference 9 were later used as a baseline comparison for two reasons. First, reference 25 lacked a sufficient number of reattachment points for comparison. Data were available only for three angles of attack: 0, 2, and 4 degrees. Secondly, flow visualization data obtained in this experimental study were gathered at $Re = 1.85 \times 10^6$ and 0.84×10^6 . Reattachment data provided in reference 25 were obtained at $Re = 1.4 \times 10^6$, while the data supplied in reference

9 provided experimental results for various Reynolds numbers and angles of attack matching the conditions of this study.

The reattachment points and error bounds for each point in reference 9 were calculated in the following way, figures 15, 16, and 17. On the given pressure distribution plot, the flat region of the curve for either upper or lower surface separation bubble was located. Near the end of this constant pressure region, the flow in the shear layer transitions from laminar to turbulent. Turbulent mixing allows the separated flow to reattach. This corresponds to the pressure recovery region of the curve immediately following the flat region. The distance between the last point in the constant pressure region and the first point in the pressure recovery region was marked as the most forward possible location of the reattachment line. The distance between the last point in the pressure recovery region and the next point on the curve was marked as the most aft probable location of the reattachment line. The reattachment point was then estimated to be halfway between these marked points. The error bounds were estimated to extend from the estimated reattachment point forward and aft to the two marked points as shown in figure 15.

In figure 18 a plot of the data in reference 25 is given. On the same plot, the corresponding reattachment

points calculated from the pressure coefficient profiles of reference 9 are given. The latter points lie very close to (or within the given error bound of) the former points. The error bounds of the points from reference 25 were supplied in the reference. Data reduced from references 9 and 25 are tabulated in table 7.

In figures 19, 20, 21, and 22 the reattachment points shown were calculated from the data of reference 9. The data, which is also given in table 8, will be used to compare to the results of this study. The error bound is noted to increase substantially for 6 degrees on the upper surface and -6 degrees for the lower surface. Therefore the curve connecting the plotted value at 5 degrees to the plotted value at 6 degrees has been dashed to refer to this point.

The method described above for calculating reattachment points from reference 9 loses accuracy as the angle of attack is increased past 4 degrees for the upper surface and past -4 degrees for the lower surface. At and beyond these angles, the flow past the ice shape becomes so unsteady that fairly accurate time averaged determination of reattachment point is difficult. The error could originate from three areas. First, the pressures measured in reference 9 are time-averaged by the instrumentation and perhaps less accurate in this region. Secondly, at higher angles the pressure recovery end point becomes very hard to identify in the

pressure plots of reference 9. Thirdly, due to lack of data points for comparison, the data of reference 9 was not calibrated for angles larger than 4 degrees and less than 0 degrees. This means that there was no calibrated data near the stall angles. Therefore, the reduced data at or near the stall angles had to be compared to data which was calibrated only between 0 and 4 degrees.

Tuft Flow Visualization: Comparison of the flow visualization reattachment data and those reported in reference 9 for Reynolds number of 0.85×10^6 are in very good agreement as figures 23 and 24 indicate. However, for data points at 6 degrees angle of attack for the upper surface and -4 and -5 degrees angle of attack for the lower surface a large discrepancy exists. This could be due to the fact that at these angles the flow is highly unsteady for each surface. This causes the reattachment point to oscillate forward and backward to a point where an accurate determination of a reattachment point is not possible from the flow visualization. The pressure data are also questionable at the angles of attack near stall, as discussed earlier. The data points reduced for the 6 degrees case, however, fall within the error bounds calculated earlier. Therefore, they should be regarded as acceptable.

Splitter Plate Flow Visualization: Figures 25 and 26 show the plots of the reattachment points compared to the data of reference 9. They are in good agreement with the reference data. The experimental results of this study have a small deviation from the data of reference 9. This deviation increases as the angle of attack increases in the negative direction for the lower surface and in the positive direction for the upper surface. The cause for this may be due in part to the effect of the unsteady separation bubble on the oil. The unsteady bubble moves back and forth, therefore leaving a smeared region to be interpreted as the reattachment line. On the lower surface, the same pattern is developed for higher negative angles of attack. This, along with the problems associated with the pressure data when the bubble is large, result in the discrepancy seen in figures 25 and 26.

Oil Flow Visualization: The reattachment points calculated through oil flow analysis are plotted in figures 27 and 28 and compared with data of reference 9. They are in close agreement with the results of reference 9 for Reynolds number of 1.85×10^6 . The calculated points for the upper surface follow the comparison graph very closely except at 6 degrees angle of attack. This point however, also lies well within the error bounds. On the lower surface a larger

discrepancy between the flow visualization results and those of reference 9 is observed. A reason for this discrepancy may be that the separation bubble itself is unsteady. This results in a chordwise movement of the bubble and a smeared region which is interpreted as the reattachment line. As mentioned earlier, another reason could be the problem associated with the pressure measurement method at angles close to the stall angle.

As the angle of attack is increased past 3 degrees for the upper surface and decreased past -1 degrees for the lower surface, a new pattern becomes visible in the photographs. This new pattern in plate of figure 29 is indicated by a band of oil mixture running in the spanwise direction. The thickness of this band of oil mixture on the leading edge grows in the chordwise direction with an increase in the airfoil angle of attack.

Cebeci [17] has applied his interactive boundary layer technique to the problem of airfoil icing. The plot in figure 29 is a part of the results presented in reference 17. It represents skin friction values versus chord location for the upper surface of a NACA 0012 model with a 5 minute simulated glaze ice at 6 degrees angle of attack.

The skin friction plot compares with the oil flow photograph in that the oil flow texture follows the same pattern as the skin friction plot. Starting near the

leading edge, and moving towards the trailing edge, about 4 percent chord the graph indicates a region of low skin friction followed by a region of high skin friction, at 8 percent chord. This is followed again by a region of low skin friction from 23 percent chord to 36 percent chord. The very same pattern described above can be traced on the oil flow photograph for the 6 degrees upper surface case. The regions of low shear are recognized by smooth oil texture while the regions of high shear show as a rough oil texture on the airfoil surface.

If the point which corresponds to zero skin friction on the skin friction plot could be taken as the reattachment point, then the calculated reattachment point of reference 17 does not match with this experiment's findings. According to the graph, reattachment occurs close to 23 percent chord. The oil flow result for the same case is close to 34 percent chord with ± 4.75 percent chord error bound. Tuft flow results indicate a reattachment value of 33 percent chord with ± 7 percent error bound. Taking into account the unsteady nature of the phenomena under study at 6 degrees angle of attack, the computational skin friction results of reference 17 should be regarded as very promising.

Comparison of Experimental Data of This Study: Figures 30 and 31 compare the experimental data obtained in this study for the upper and lower surfaces with that of reference 9. Figure 31 shows that for angles of attack of zero and higher, on the lower surface, the experimental data are less scattered than for negative angles. This could be due to the fact that at higher angles (positive angles) the separation bubble on the lower surface ice horn becomes very small and it is easier to detect in the photos compared to negative angles. The same argument can be applied for the upper surface set at lower angles (negative angles) of attack. Altogether, figures 30 and 31 show that all three different flow visualization methods give similar results for the reattachment line.

In general, all of the flow visualization data compare well with the data of reference 9 up to -2 degrees for the lower surface and up to 4 degrees for the upper surface. The comparison, as figures 30 and 31 indicate, shows an increasing discrepancy past -2 degrees for the lower surface and past 4 degrees for the upper surface. This supports the idea that the data reduction scheme for reference 9 which was described earlier is not very accurate for angles close to the stall angle.

V. Conclusions and Recommendations

Various methods of flow visualization have been employed in this study to highlight the flow field about the leading edge of an airfoil with simulated glaze ice. The tests were conducted on a NACA 0012 model with a five minute leading edge glaze ice simulation in the OSU 3x5 foot subsonic wind tunnel.

At positive angles of attack, the bubble on the upper surface was seen to have a larger size, while at negative angles of attack (nose down), the same bubble had negligible size. The reverse of this fact was seen to be true for the lower surface, i.e. at negative angles the leading edge separation bubble was larger and at positive angles, the bubble reduced in size.

The results obtained from this study were reduced to the form of reattachment line plots. These plots were later compared to the experimental data of Bragg [9,25] and the computational results of Cebeci [17]. In general, the experimental findings of this study matched all other comparison data. While the method of tuft flow visualization proved to correlate better to the results of Bragg, the splitter plate and the oil flow visualization method showed more discrepancy from the comparison data. The method of oil flow highlighted

certain aspects of the leading edge flow field which was predicted by the computational results. The computational findings were shown to be in fair agreement with experiment.

The method of smoke flow visualization provided very good qualitative information and proved to be more informative when recorded on video instead of still photographs. The method of liquid crystal flow visualization provided a new and dynamic method of flow visualization. The results obtained from this method, however, were not conclusive enough to be compared against other data.

Flow visualization can be used to reveal a great deal about the flow field dynamics of an airfoil. With proper application of various methods of flow visualization the flow field about an airfoil with a complex flow field, such as the one with a leading edge glaze ice simulation, can be quantitatively visualized. Since the flow is highly unsteady at the angles at and beyond which the flow separates from the airfoil, a method of flow visualization which is more suitable for unsteady flow situations should be employed. The method employing liquid crystals shows great potential. More research on the characteristics of this substance is needed, however, before quantitative results can be obtained. Digitizing the flow [26], after it has been seeded with certain tracing particles, is another method

that can possibly shed more light on the unsteady aspect of the problem.

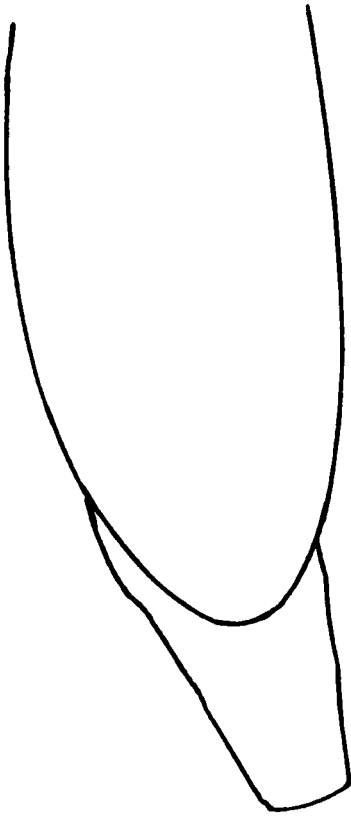
On the other side of the spectrum, more detailed separation data are needed before more accurate comparisons can be made. A denser arrangement of velocity profile measurements similar to those reported in reference 25 will serve as a good basis for future comparison. In this manner, correlations to pressure distribution profiles can be avoided entirely and more accurate reattachment line profiles can be obtained.

LIST OF REFERENCES

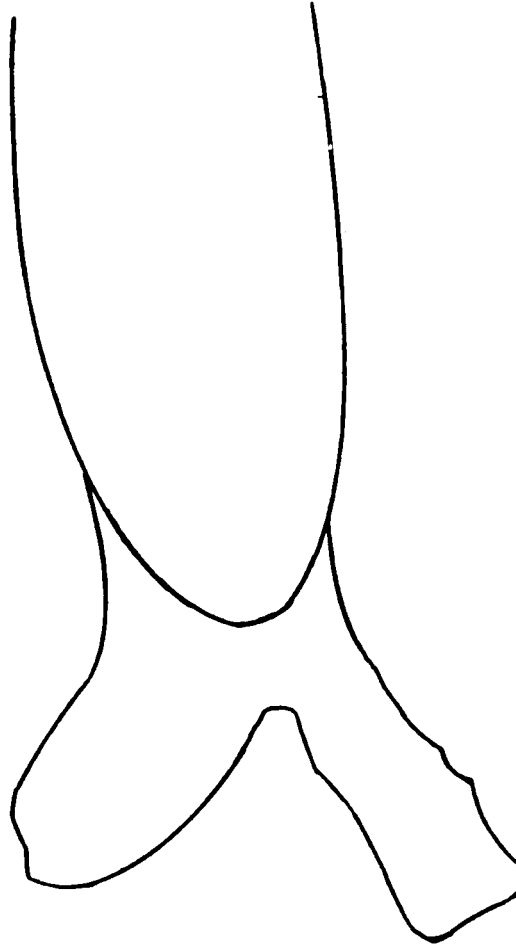
- 1) Bragg, M. B., Gregorek, G. M. and Lee, J. D., "Airfoil Aerodynamics in Icing Conditions", Journal of Aircraft, Vol. 23, No.1, January 1986
- 2) Gray, Vernon H., "Prediction of Aerodynamic Penalties Caused by Ice Formation on Various Airfoils", NASA TN D-2166, February 1964
- 3) Gray, Vernon H. and Von Glahn, Uwe H., "Aerodynamic Effects Caused by Icing of an Unswept NACA 65A004 Airfoil", NACA TN 4155, 1958
- 4) Bragg, M. B., Zaguli, R. J. and Gregorek, G. M., "Wind Tunnel Evaluation of Airfoil Performance Using Simulated Ice Shapes", NASA CR 167960, November 1982
- 5) Shaw, Robert J. and Sotos, Ray G., "An Experimental Study of Airfoil Icing Characteristics", NASA TM 82790, January 1982
- 6) Bragg, M. B., "Predicting Airfoil Performance with Rime and Glaze Ice Accretions", AIAA Paper No. 84-0106, presented at the 22nd Aerospace Sciences Meeting, Reno, Nevada, January 9-12, 1984
- 7) Bragg, M. B. and Coirier, W. J., "Detailed Measurements of the Flow Field in the Vicinity of an Airfoil with Glaze Ice", AIAA Paper No. 85-0409, presented at the 23rd Aerospace Sciences Meeting, Reno, Nevada, January 14-17, 1985
- 8) Bragg, M. B. and Coirier, W. J., "Aerodynamic Measurements of an Airfoil with Simulated Glaze Ice", AIAA Paper No. 86-0484, presented at the 24th Aerospace Sciences Meeting, Reno, Nevada, January 6-9, 1986
- 9) Bragg, M. B., "An Experimental Study of the Aerodynamics of a NACA 0012 Airfoil with a Simulated Glaze Ice Accretion", Research Foundation Report No. 712620/762009, The Ohio State University, Columbus, Ohio, November 1986
- 10) Horton, H. P., "A Semi-Empirical Theory for the Growth and Bursting of Laminar Separation Bubbles", Aeronautical Research Council Current Papers No. 1073, June 1967

- 11) Gaster, M., "The Structure and Behavior of Laminar Separation Bubbles", Separated Flows II, AGARD Conference Proceedings No. 4, Part 2, presented at AGARD Fluid Dynamics Panel Meeting on Separated Flows, pp. 813 - 854, Rhode-Saint-Genese, Belgium, May 10-13, 1966
- 12) Crimi, Peter and Reeves, Barry L., "Analysis of Leading Edge Separation Bubbles on Airfoils", AIAA Journal, Vol. 14, No. 11, December 1976
- 13) Carter, James E., "Solutions for Laminar Boundary Layers with Separation and Reattachment", AIAA Paper No. 74-583, presented at the 7th Fluid and Plasma Dynamics Conference, Palo Alto, California, June 17-19, 1974
- 14) Briley, Roger W. and McDonald, Henry, "Numerical Prediction of Incompressible Separation Bubbles", Journal of Fluid Mechanics, Vol. 69, Part 4, pp. 631-656, 1975
- 15) Zaguli, R. J., "Potential Flow Analysis of Glaze Ice Accretions on an Airfoil", M.S. Thesis, The Ohio State University, Columbus, Ohio, 1983
- 16) Laschka, B., Jesse, R. E., "Ice Accretion and Its Effects on Aerodynamics of Unprotected Aircraft Components", Aircraft Icing, AGARD Advisory Report No. 127, presented at AGARD Fluid Dynamics Panel Roundtable Discussion on Aircraft Icing, Ottawa, Canada, September 30, 1977
- 17) Cebeci, Tuncer, "Interactive Boundary-Layer Analysis of Iced Airfoils", presented at Airfoil Performance-in-Icing Workshop, NASA Lewis Research Center, July 17-18, 1986
- 18) Potapczuk, Mark, "Numerical Analysis of a NACA 0012 Airfoil with Leading Edge Ice Accretions", AIAA Paper No. 87-0101, presented at the 25th Aerospace Sciences Meeting, Reno, Nevada, January 12-15, 1987
- 19) Tang, W. and Sankar, N. C., "Navier-Stokes Solutions for Airfoils with Simulated Ice Shape", presented at Airfoil Performance-in-Icing Workshop, NASA Lewis Research Center, July 17-18, 1986
- 20) Freymouth, P., Bank, W., Palmer, M., "Use of Titanium Tetrachloride for Visualization of Accelerating Flow Around Airfoils", Flow Visualization III, ed: W. J. Yang, Hemisphere 1983, pp. 99 - 105

- 21) Mueller, T. J., "Smoke Flow Visualization", Lecture Series on Visualization and Optical Measurement of Fluid Flows, presented at Texas A & M University, College Station, Texas, 1983
- 22) Mueller, T. J., private communication, June 1986
- 23) Steinberg, David R., "Development of Liquid Crystal/Skin Friction Measurement Device", Flow Visualization III, ed: W. J. Yang, Hemisphere 1983, pp. 49 - 54
- 24) Holmes, B. J., Gall, P. D., Croom, C. C., Manuel, G. S., Kelliher, W. C., "A New Method for Laminar Boundary Layer Transition Visualization in Flight - Color Changes in Liquid Crystal Coatings", NASA TM 87666, January 1986
- 25) Bragg, M. B. and Spring, S. A., "An Experimental Study of the Flow Field About an Airfoil with Glaze Ice", AIAA paper No. 87-0100, presented at the 25th Aerospace Sciences Meeting, Reno, Nevada, January 12-15, 1987
- 26) Settles, Gary S., "Flow Visualization Techniques for Practical Aerodynamic Testing", Flow Visualization III, ed: W. J. Yang, Hemisphere 1983, p. 306



RIME



GLAZE

Figure 1 . Typical Rime and Glaze Ice Accretions

NACA 0012 ICING CONDITIONS

$\alpha = 4 \text{ deg.}$ $V = 130 \text{ mph}$

$\bar{d} = 20 \text{ }\mu\text{m}$ Liquid Water Content = 2.1 g/m^3

$T = 18 \text{ }^\circ\text{F}$

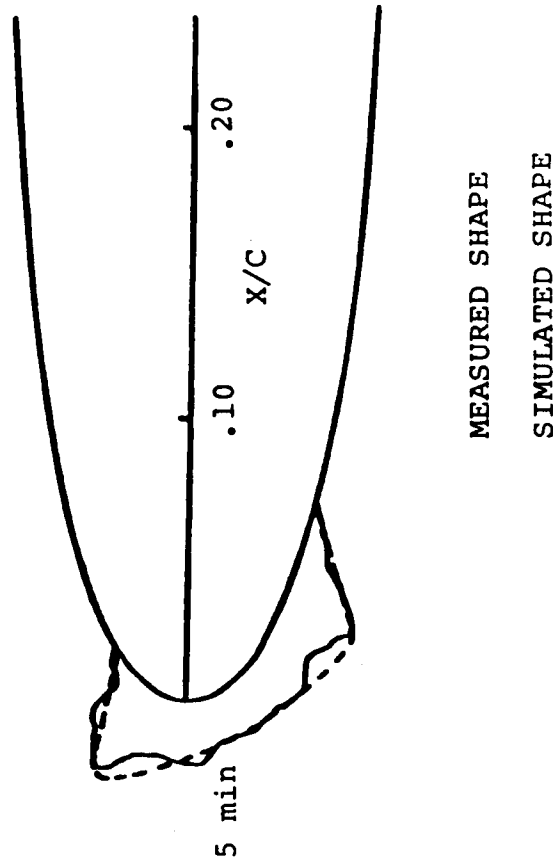


Figure 2 . Comparison of the Measured and Simulated Ice Shape.

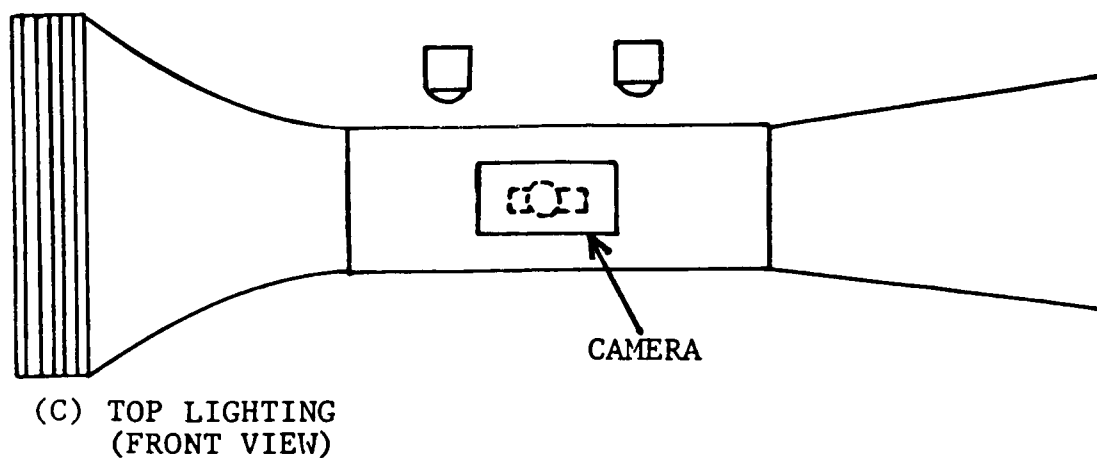
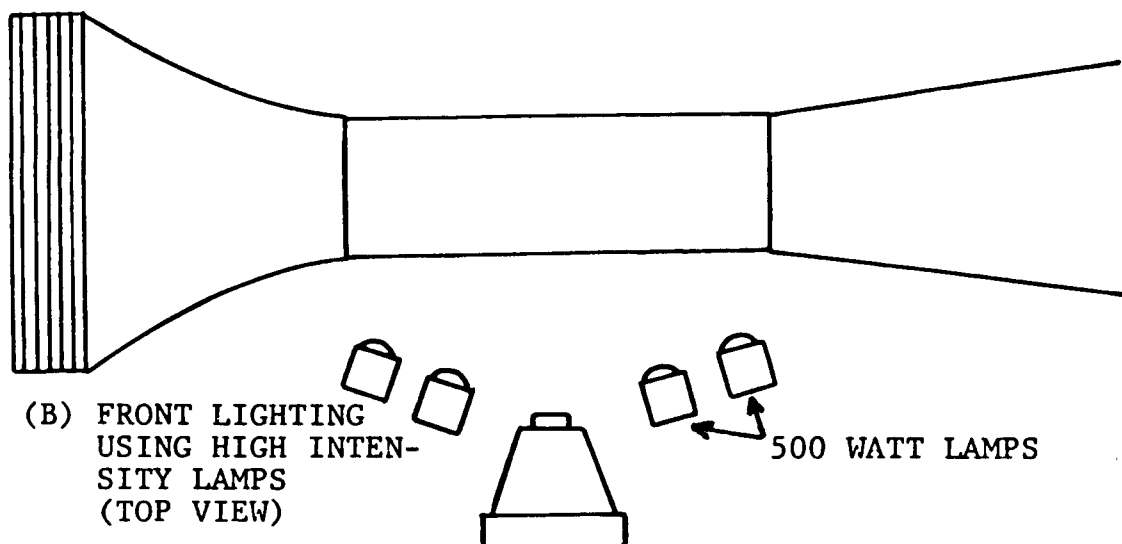
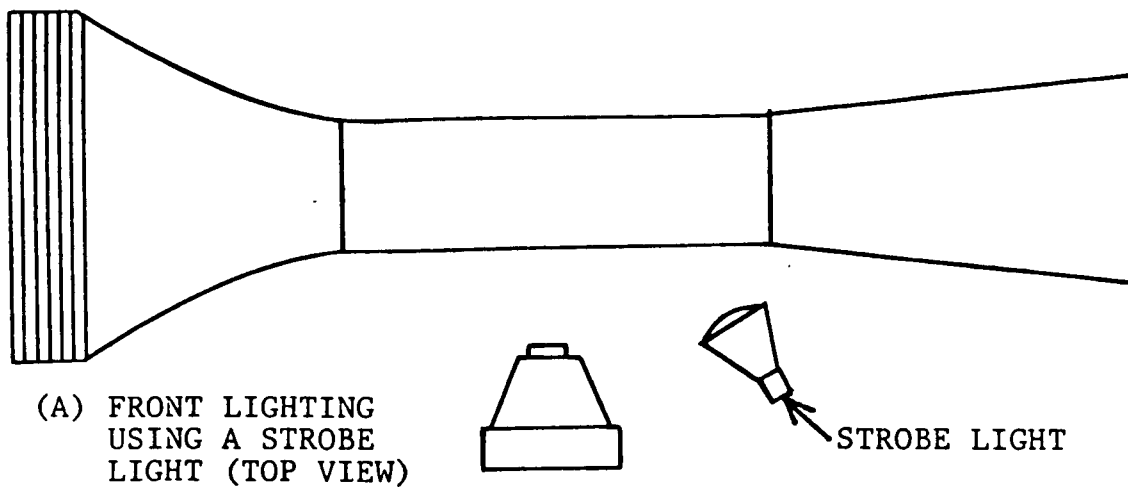


Figure 3 . Lighting and Camera Arrangements

ORIGINAL PAGE IS
OF POOR QUALITY

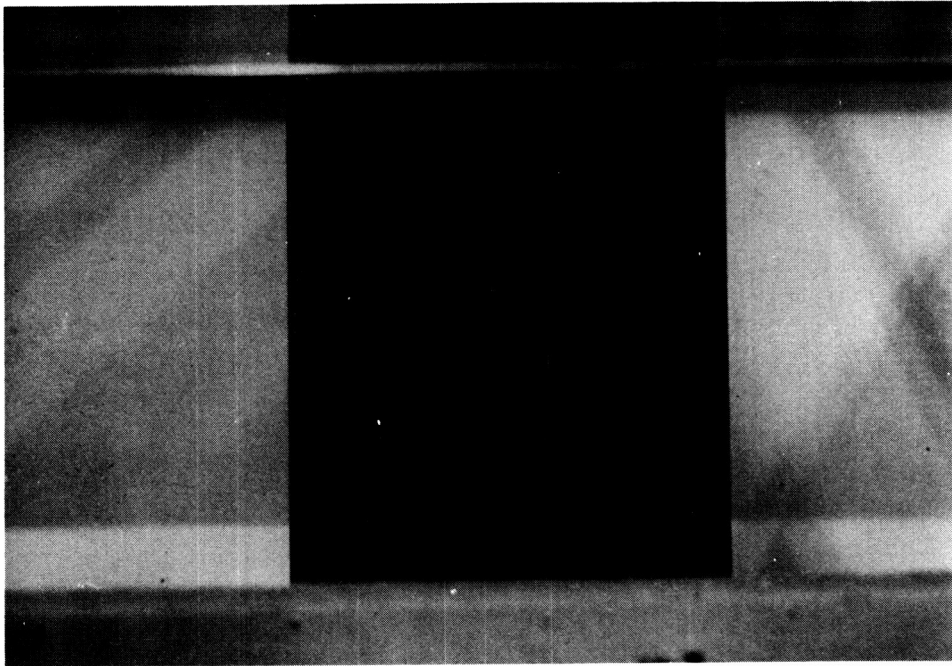


Figure 4. Tuft Arrangement on the NACA 0012 Model
with 5 Minute Simulated Glaze Ice.

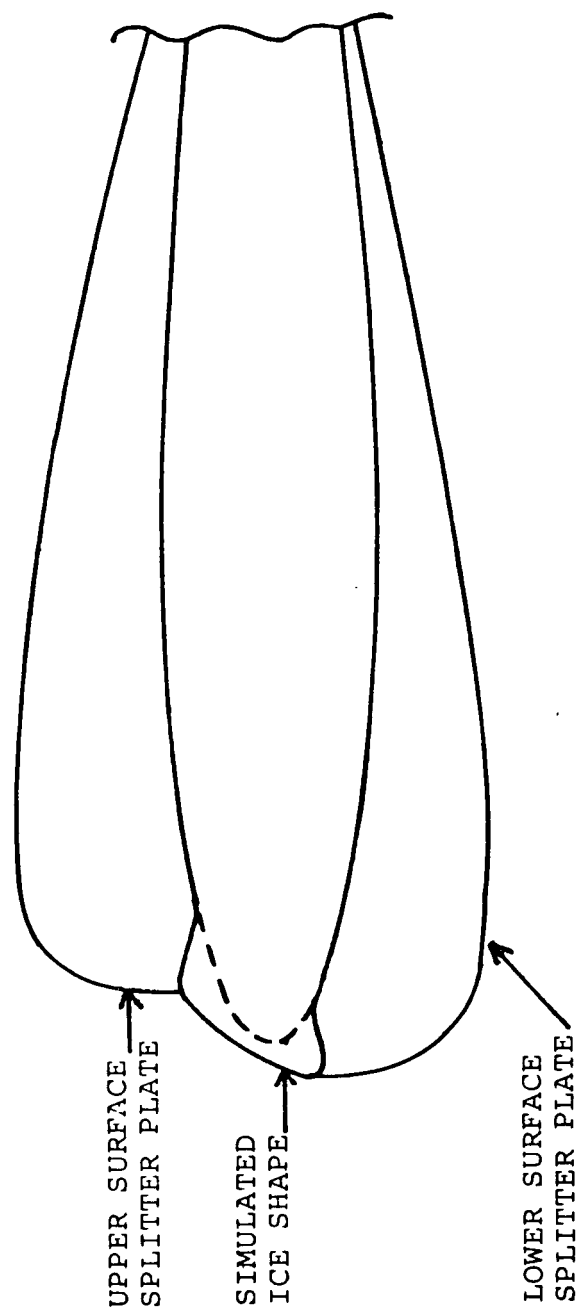


Figure 5. Splitter plate position on the NACA 0012

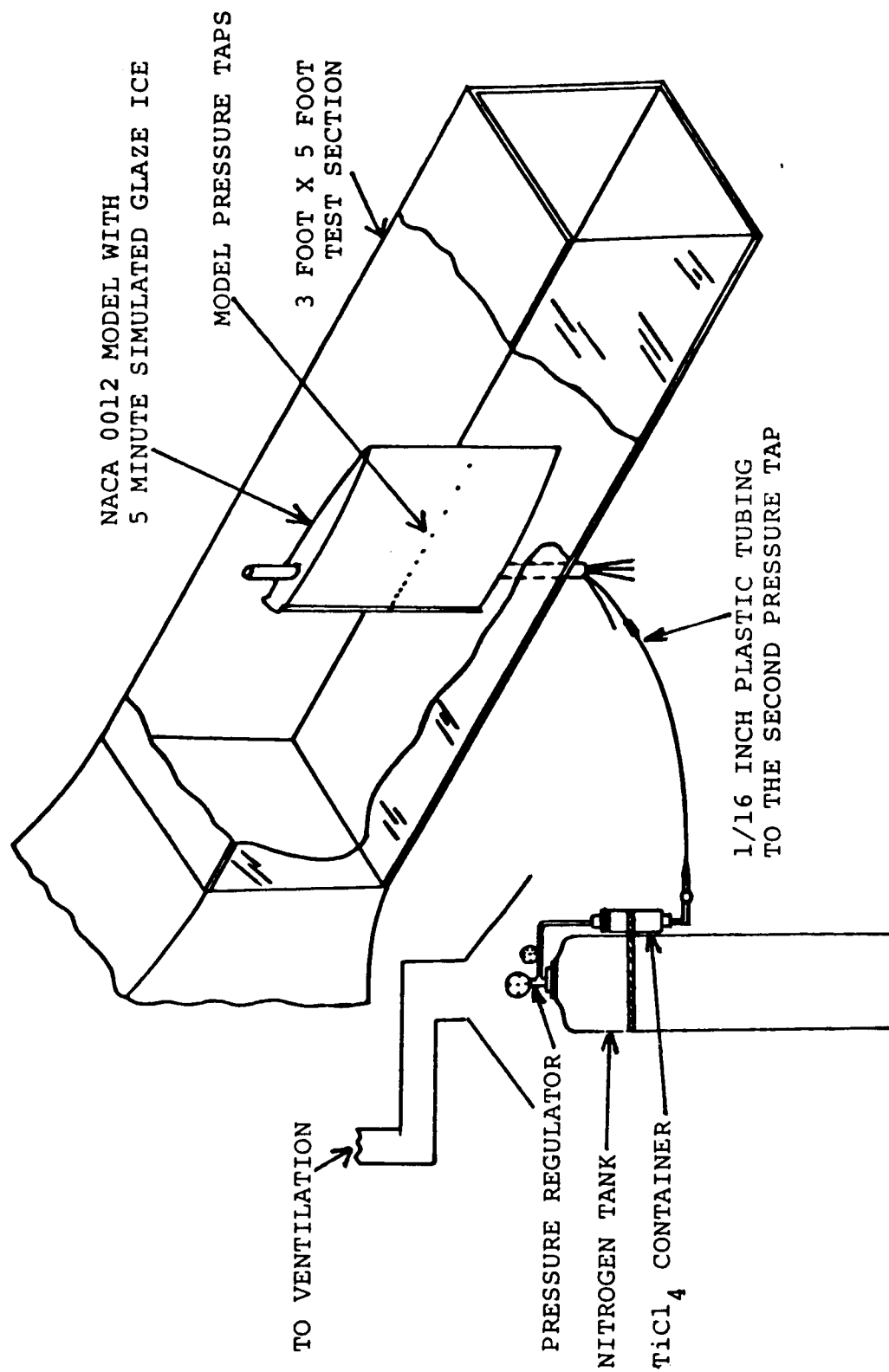


Figure 6 . Wind Tunnel Test Section and the Titanium Tetra Chloride Test Rig

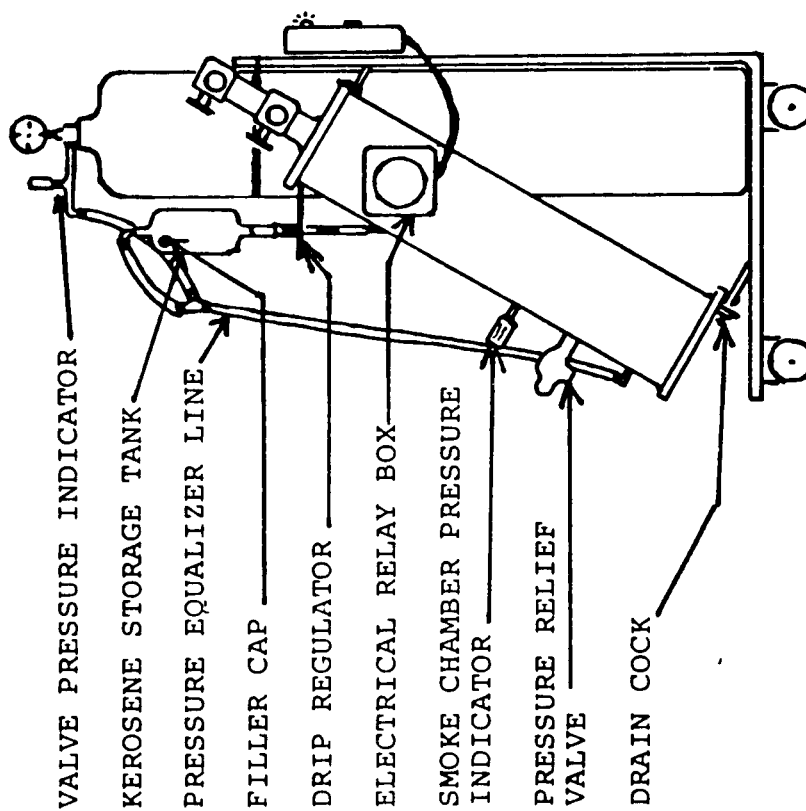
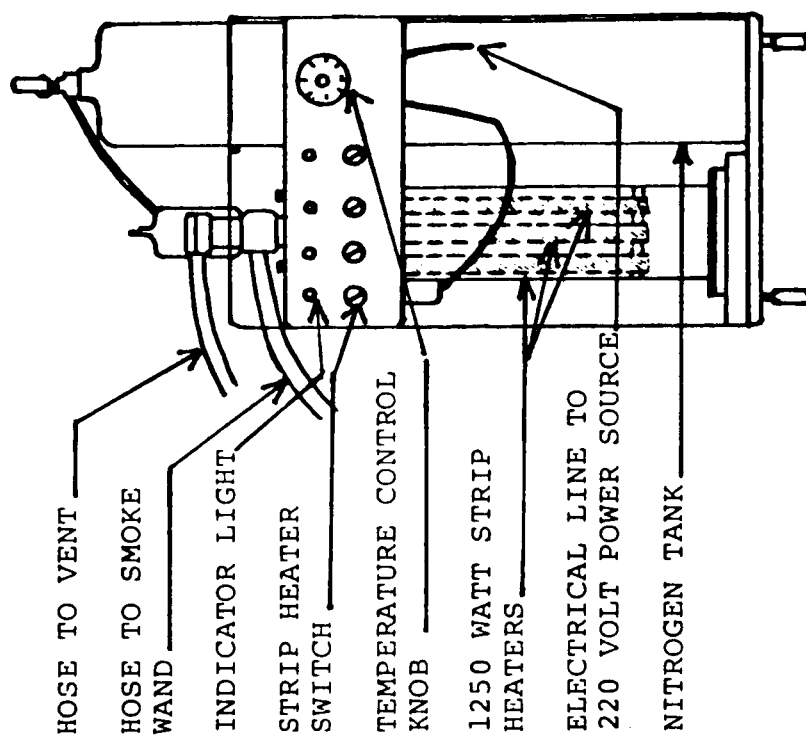
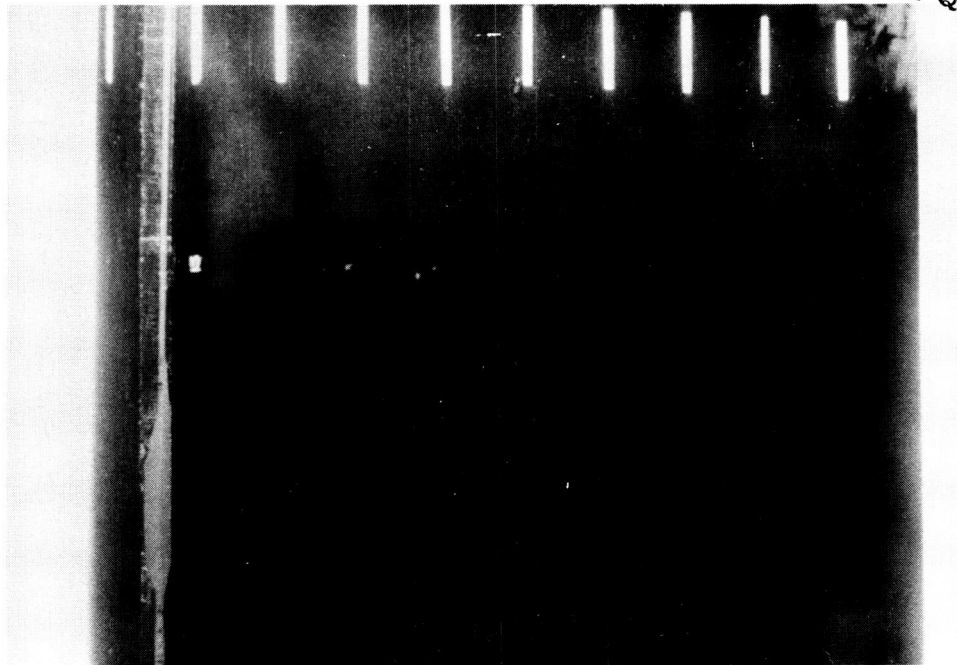


Figure 7 . Diagram of Kerosene Smoke Generator

ORIGINAL PAGE IS
OF POOR QUALITY



V = 180 fps
AOA = -2 deg, LOWER SURFACE

REATTACHMENT LOCATION

V = 180 fps, AOA = 0 deg, LOWER
SURFACE

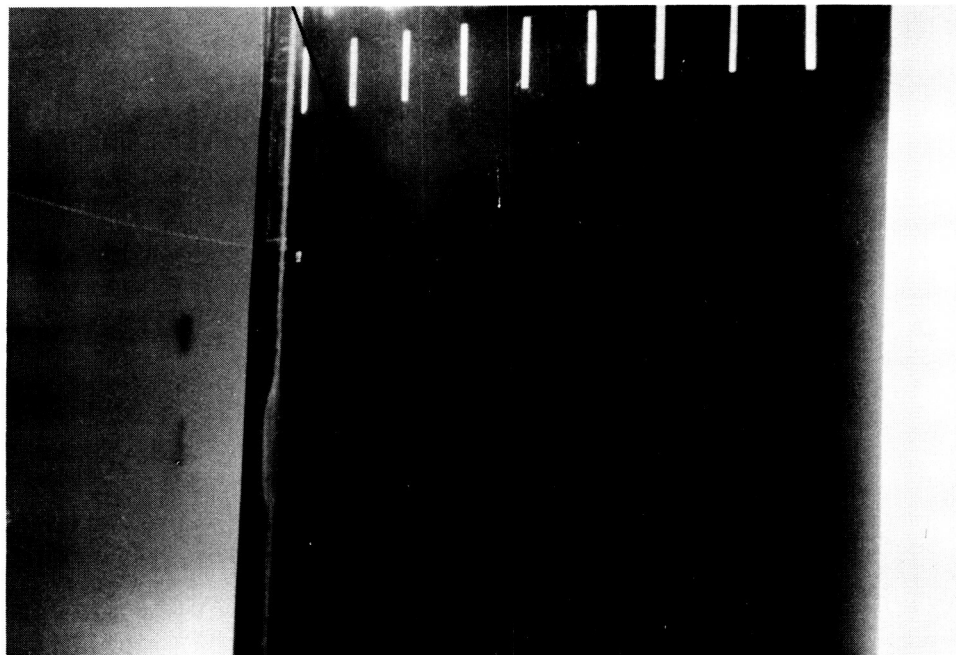


Figure 8. Liquid Crystal Flow Visualization on the
NACA 0012 with Simulated Glaze Ice.

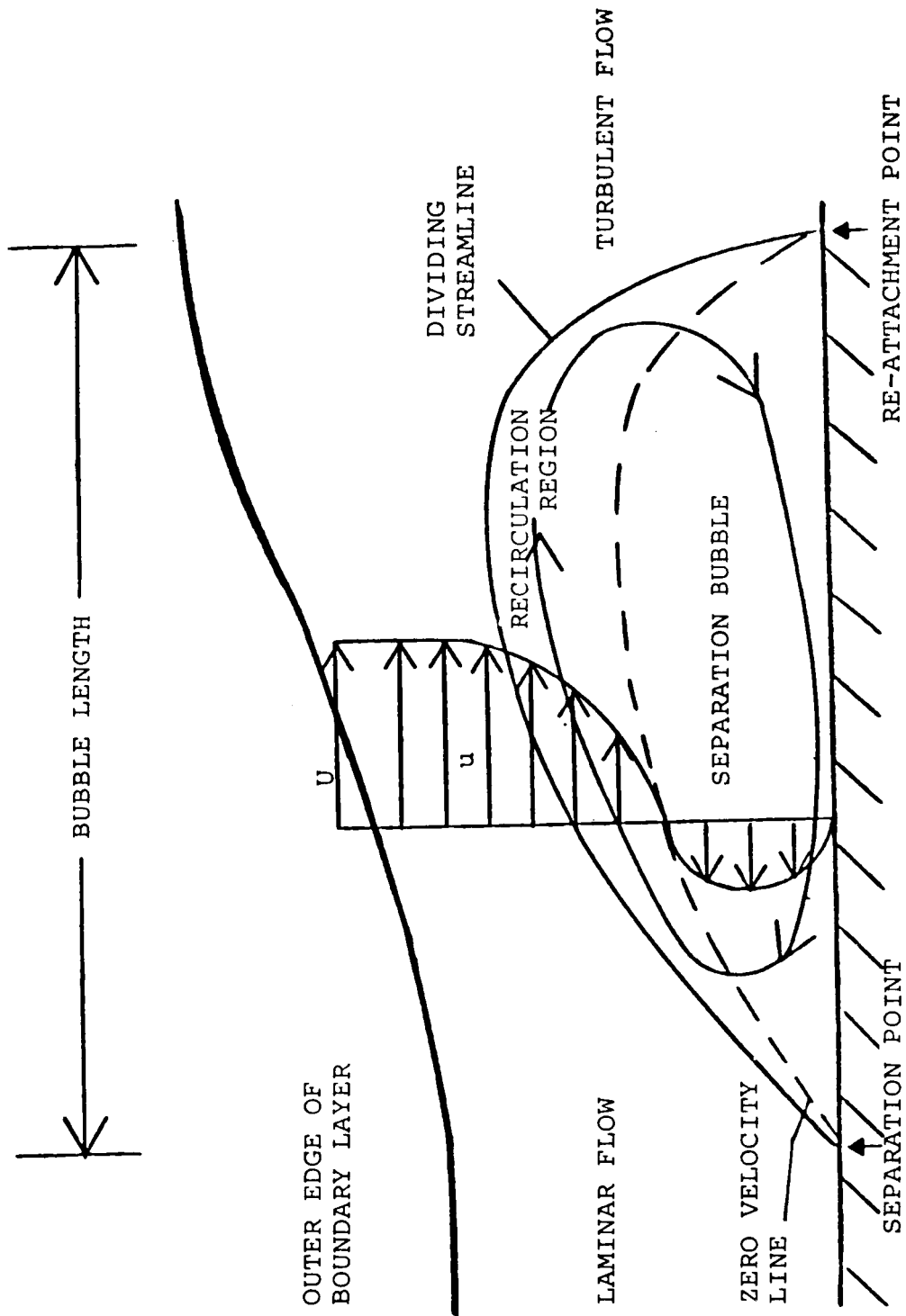
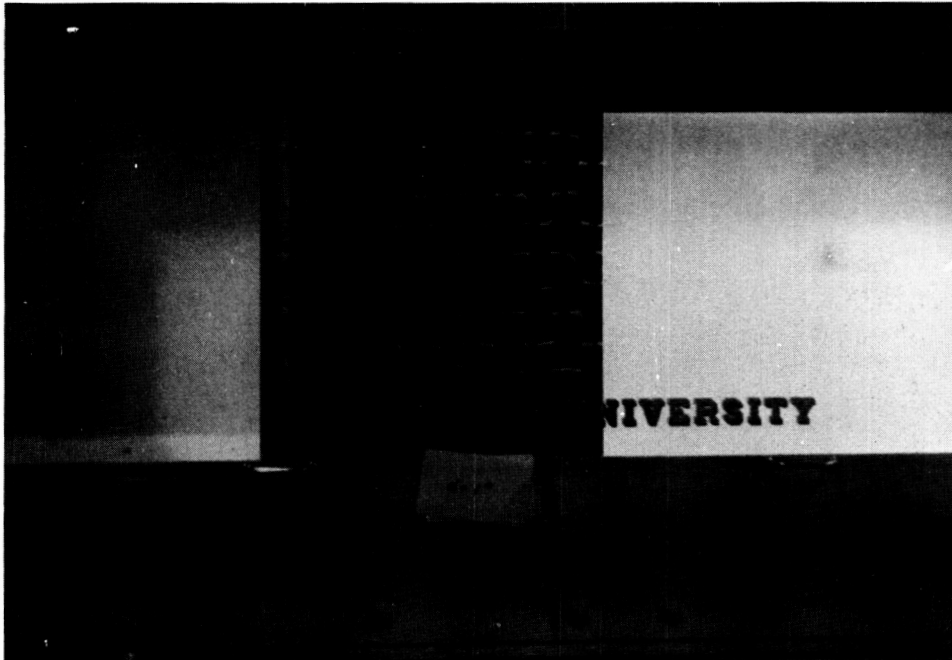


Figure 9 . Diagram of Laminar Separation Bubble



$V = 85 \text{ fps}$, $\text{AOA} = 1 \text{ deg}$, LOWER SURFACE

$V = 85 \text{ fps}$, $\text{AOA} = 7 \text{ deg}$, UPPER SURFACE

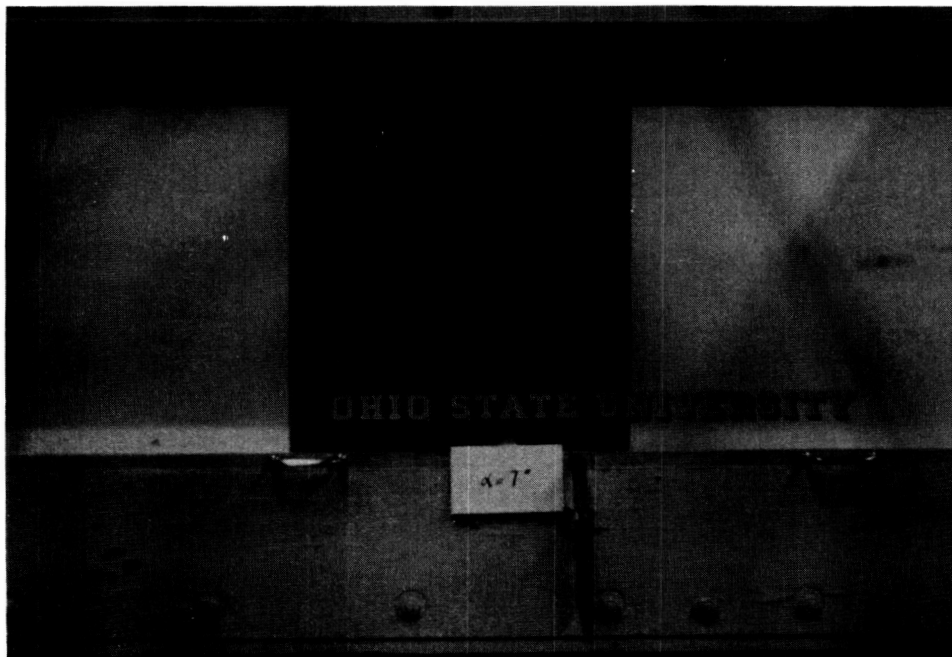
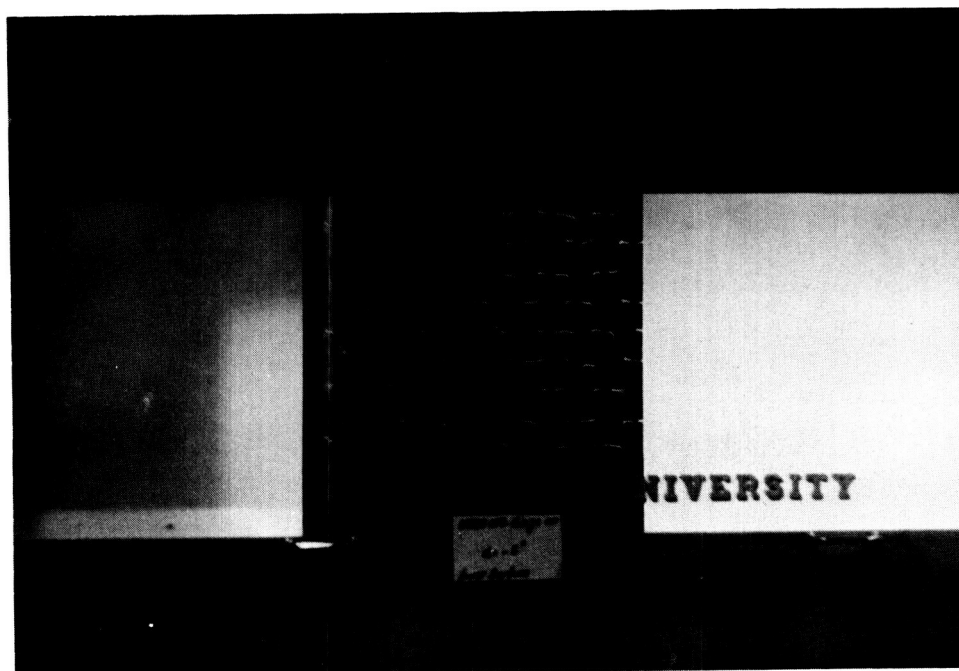


Figure 10. Tuft Flow Visualization on the NACA 0012
with Simulated Glaze Ice.

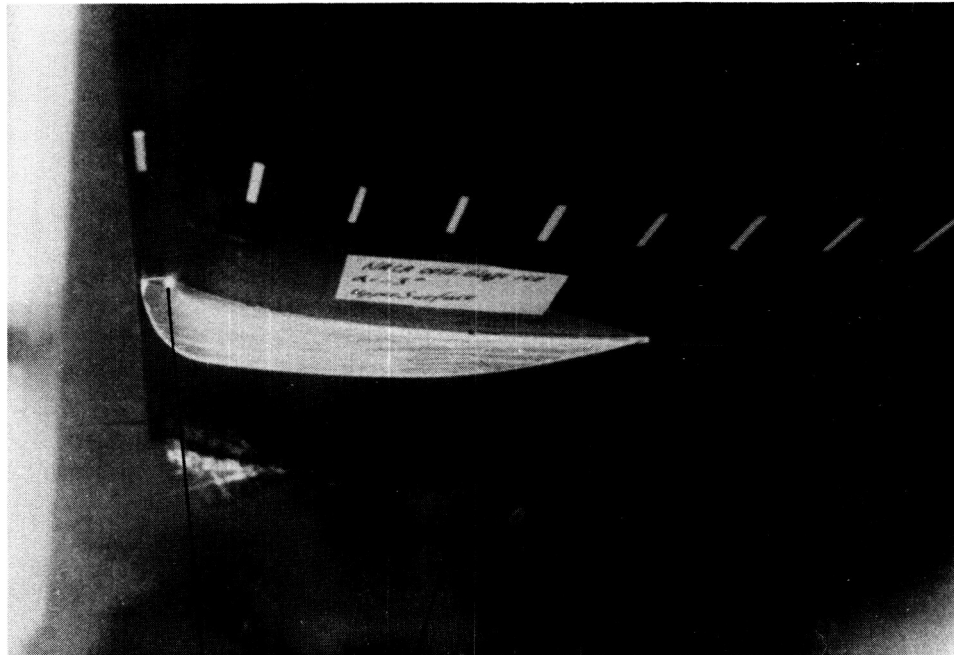



 REATTACHMENT LINE
 ERROR BOUND

Figure 11. Reattachment Line and Error Bound
 Measurement in Tuft Flow Visualization.

ORIGINAL PAGE IS
 OF POOR QUALITY

ORIGINAL PAGE IS
OF POOR QUALITY



PARALLEL STREAMLINES $V = 180$ fps
RECIRCULATING REGION $AOA = -3$ deg, UPPER SURF.

$V = 180$ fps
 $AOA = 5$ deg, UPPER SURFACE

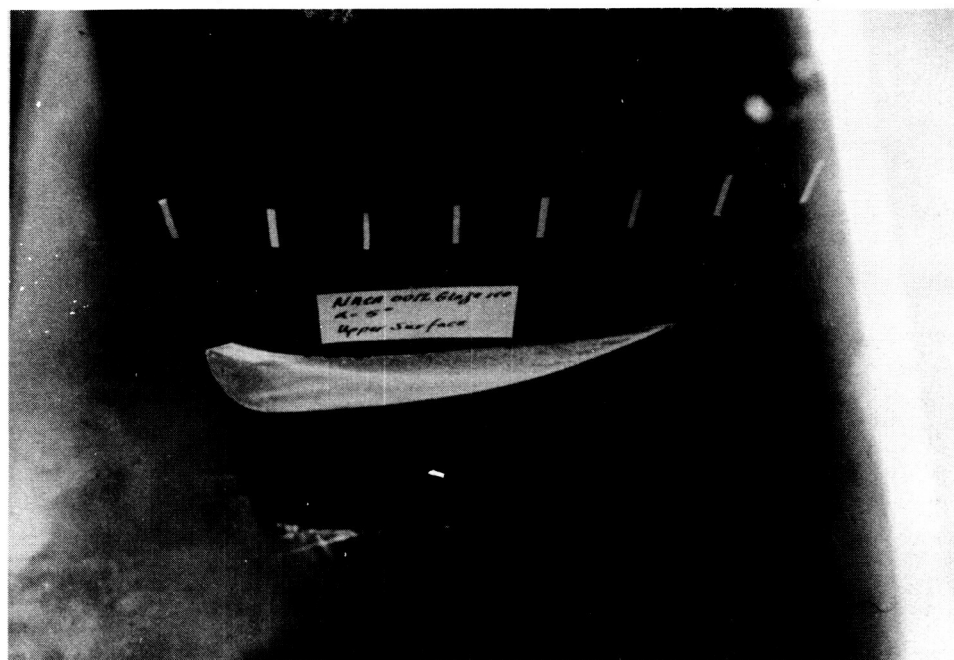


Figure 12. Splitter Plate Flow Visualization on the NACA 0012 with 5 Minute Glaze Ice.

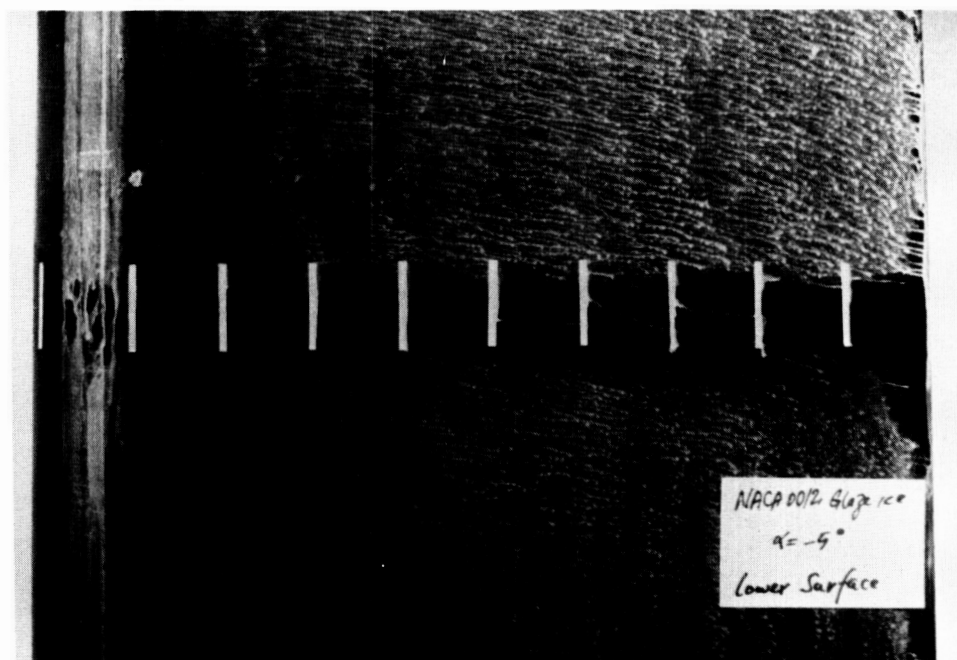
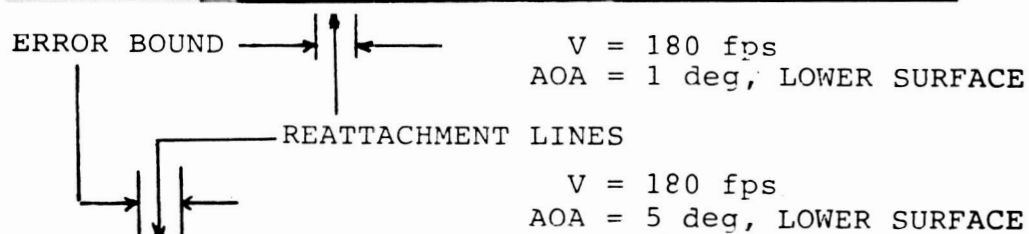
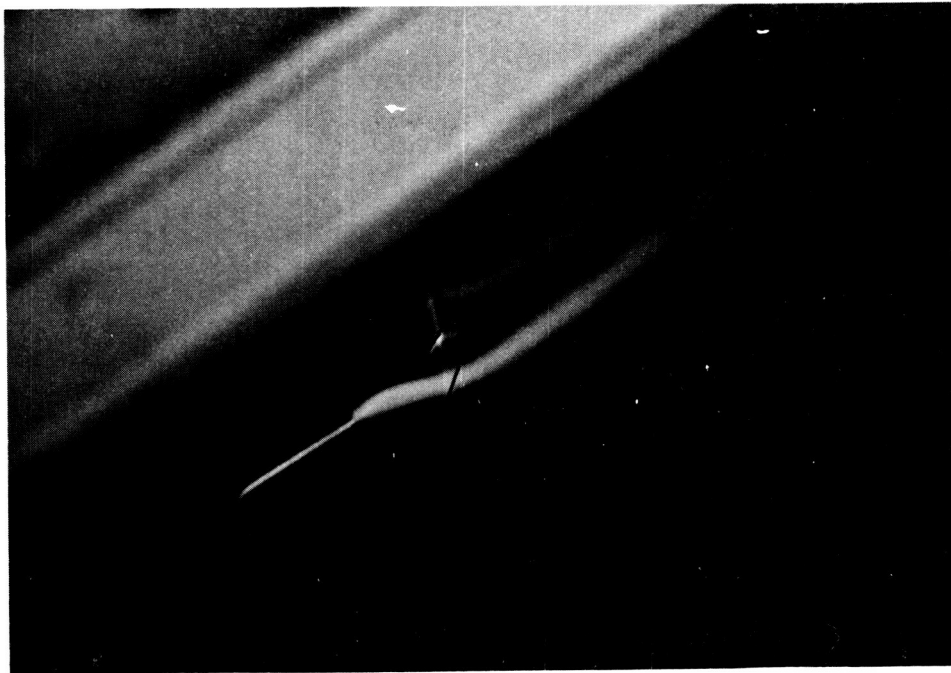


Figure 13. Oil Flow Visualization on the NACA 0012
 with 5 Minute Simulated Glaze Ice.

ORIGINAL PAGE IS
OF POOR QUALITY



SEPARATION BUBBLE REGION

V = 30 fps
AOA = 2 deg, UPPER SURFACE

V = 30 fps
AOA = -1 deg, UPPER SURFACE

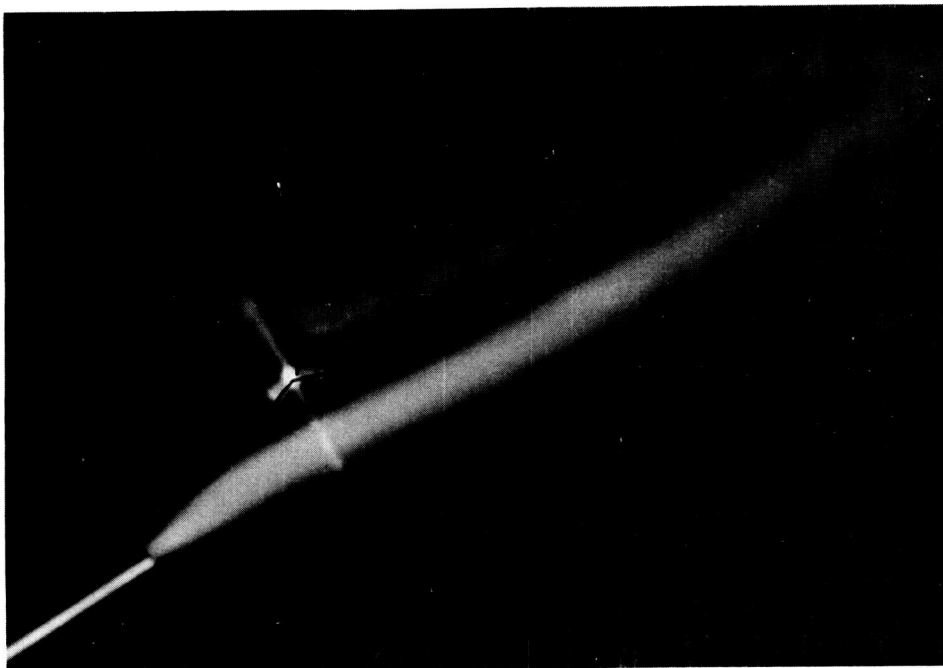


Figure 14. Smoke Flow Patterns Over the NACA 0012
with Simulated Glaze Ice.

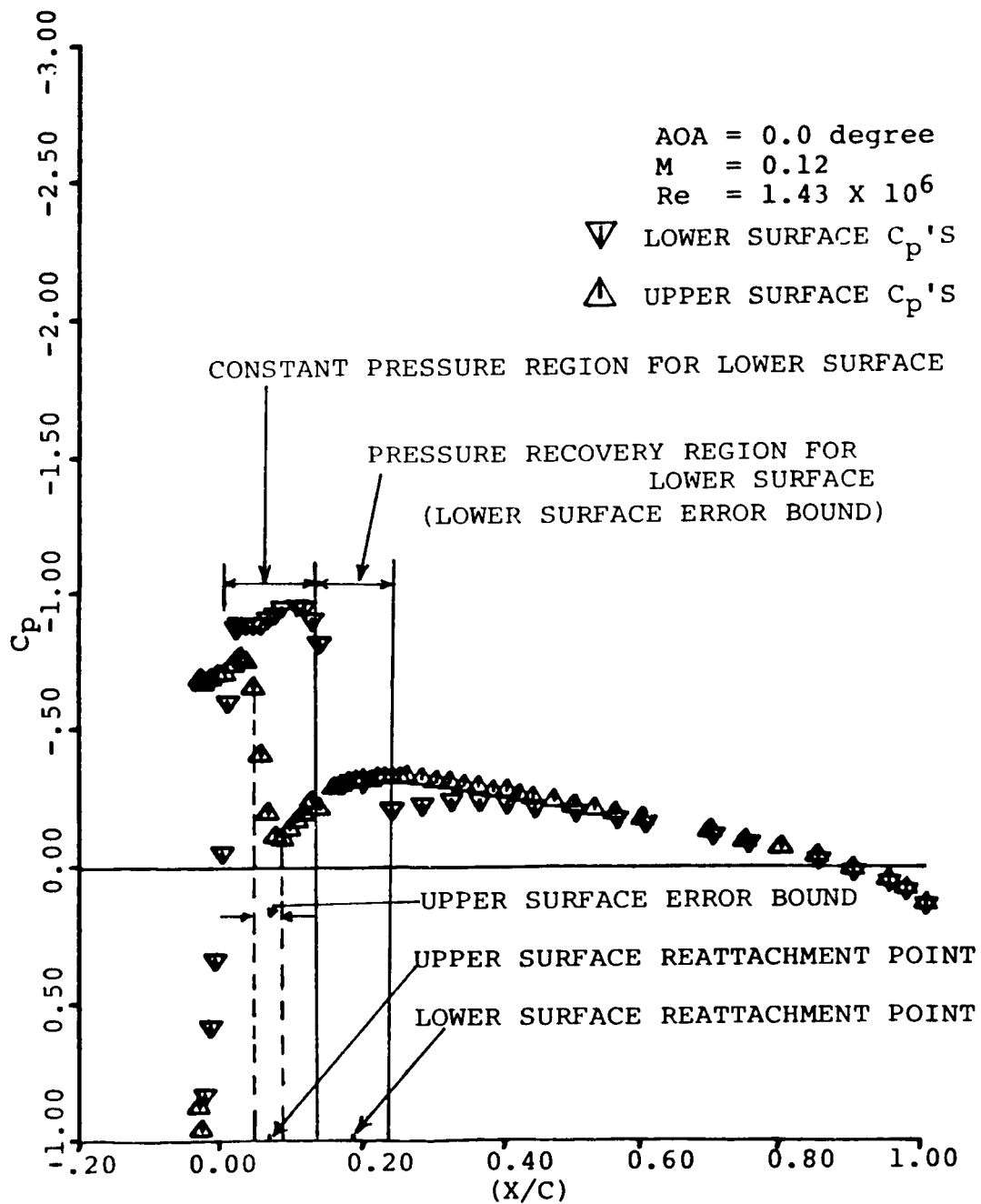


Figure 15. Error Bound and Reattachment Point Calculation from Reference 9.

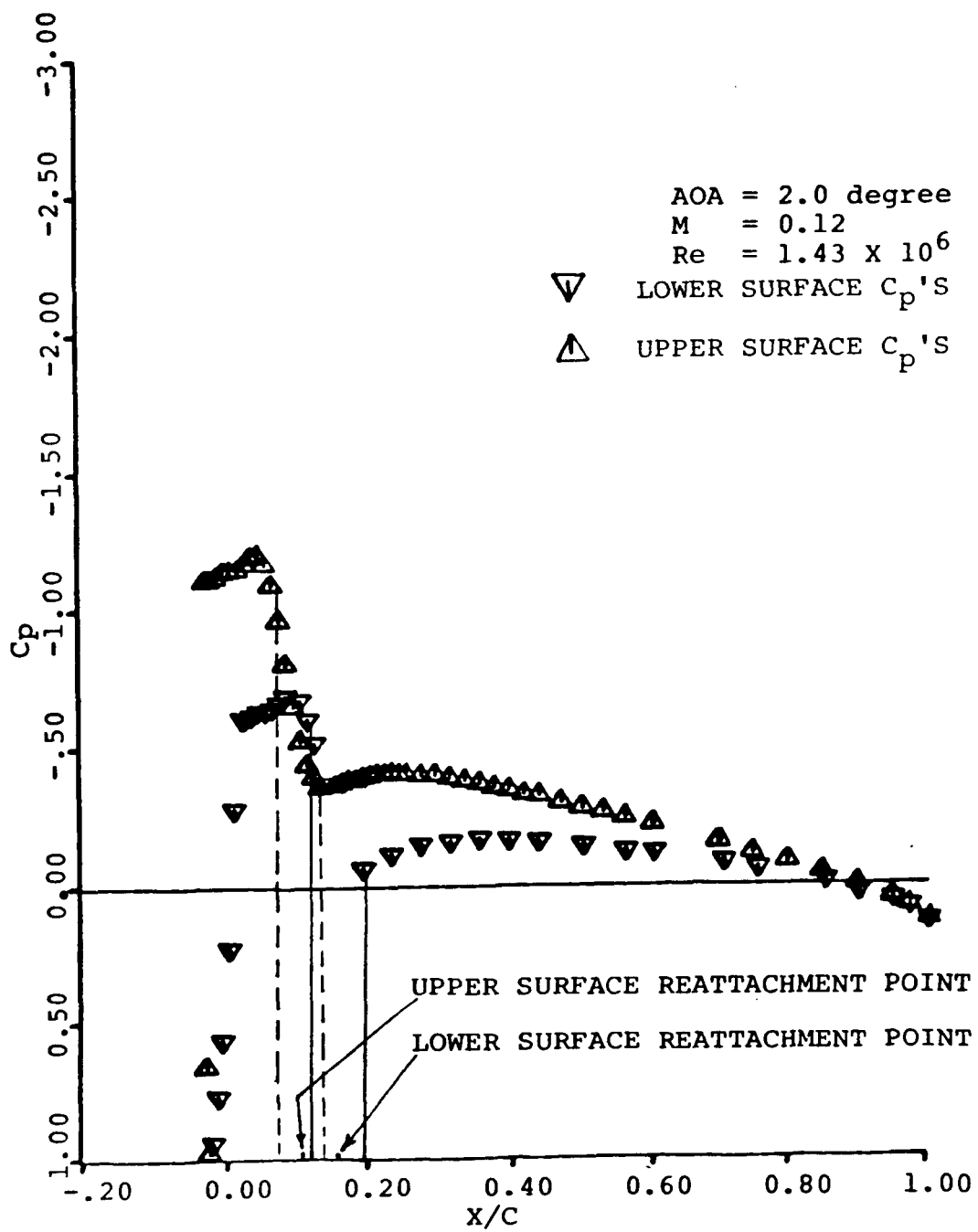


Figure 16. Error Bound and Reattachment Point Calculation from Reference 9.

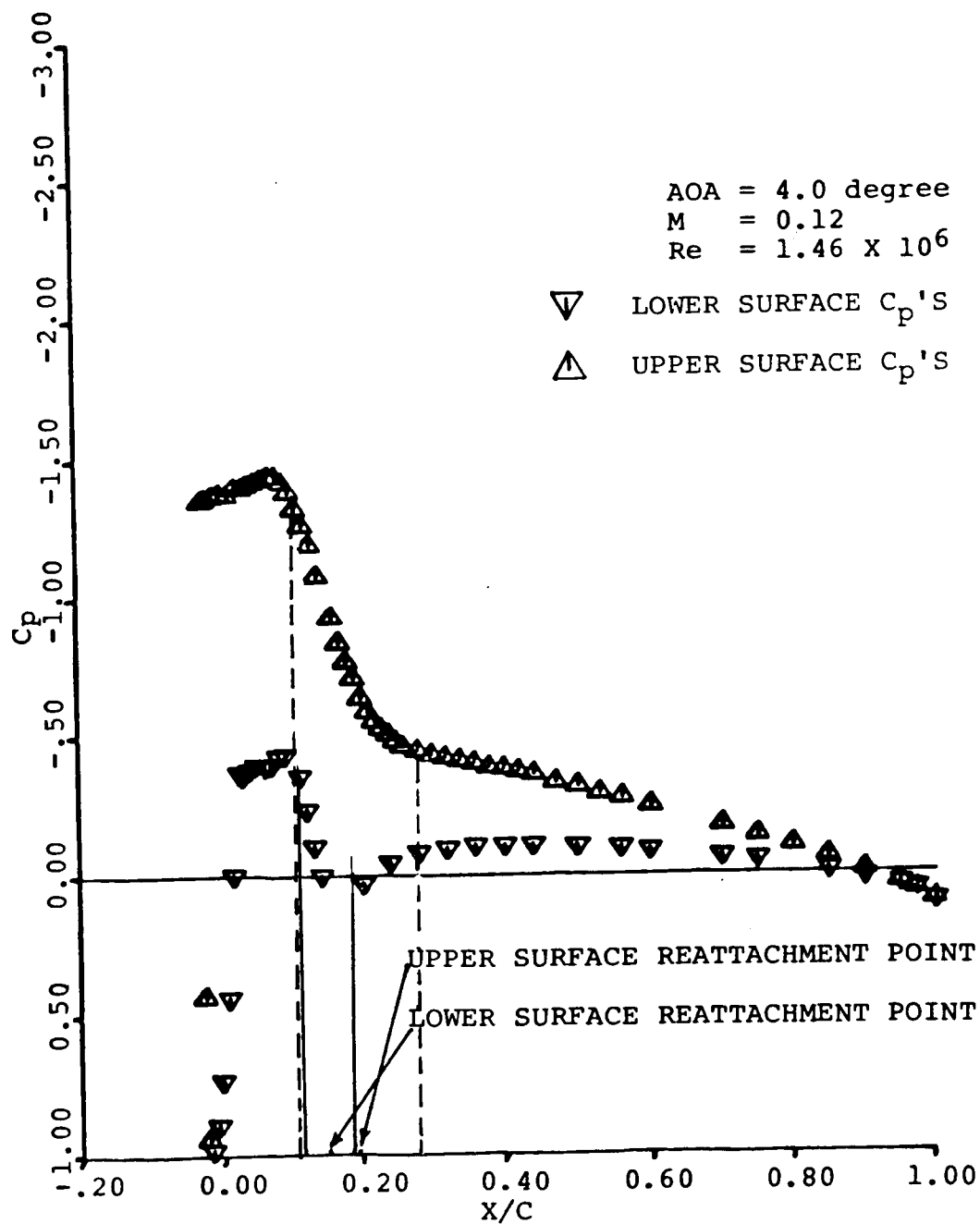


Figure 17. Error Bound and Reattachment Point Calculation from Reference 9.

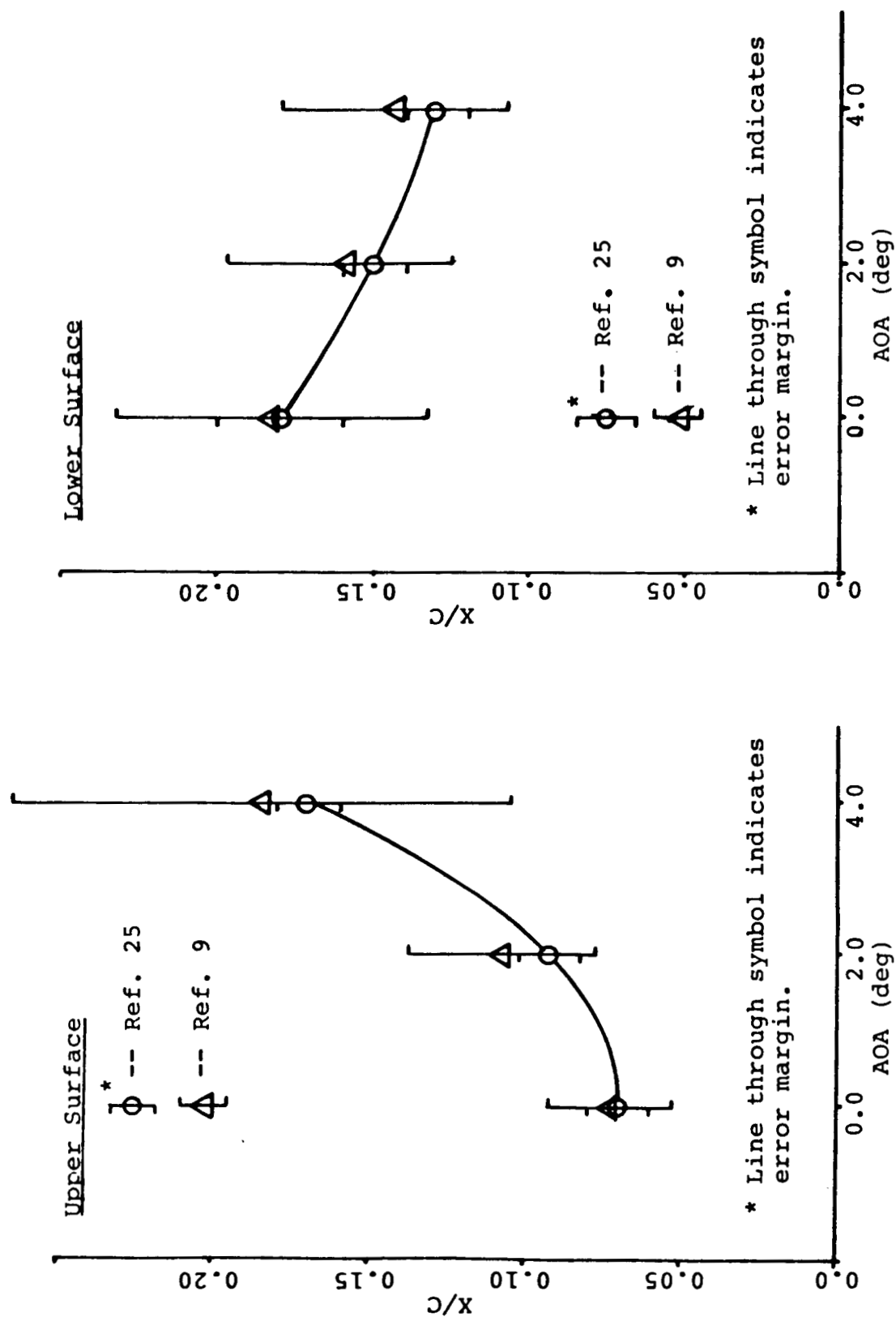


Figure 18. Upper and Lower Surface Reattachment Profiles from Measured Velocity Profiles of Reference 25 Compared with Pressure Distribution Profiles of Reference 9.

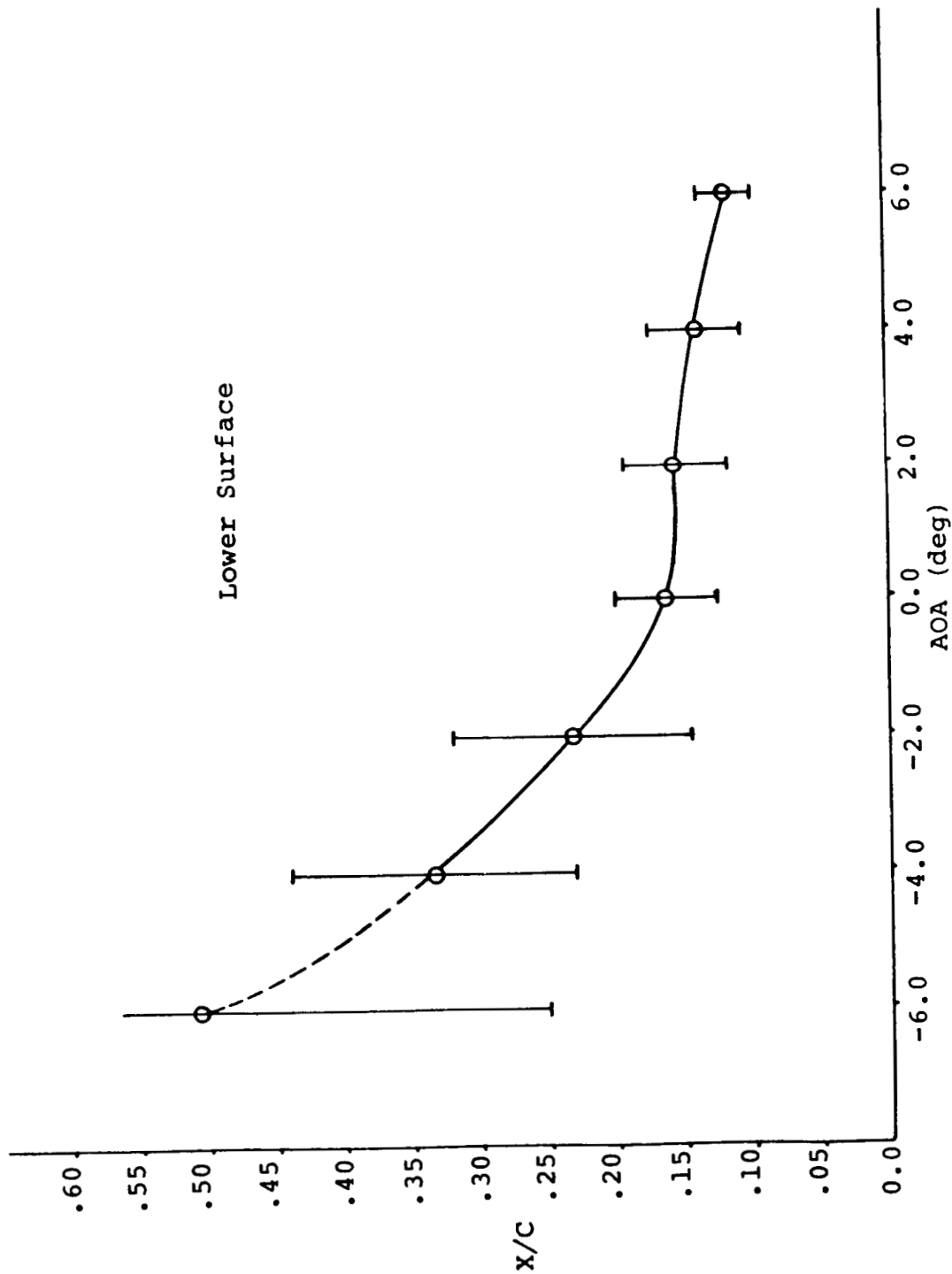


Figure 19. Reattachment Points Reduced from Pressure Plots of Reference 9 for $Re = 1.8 \times 10^6$.

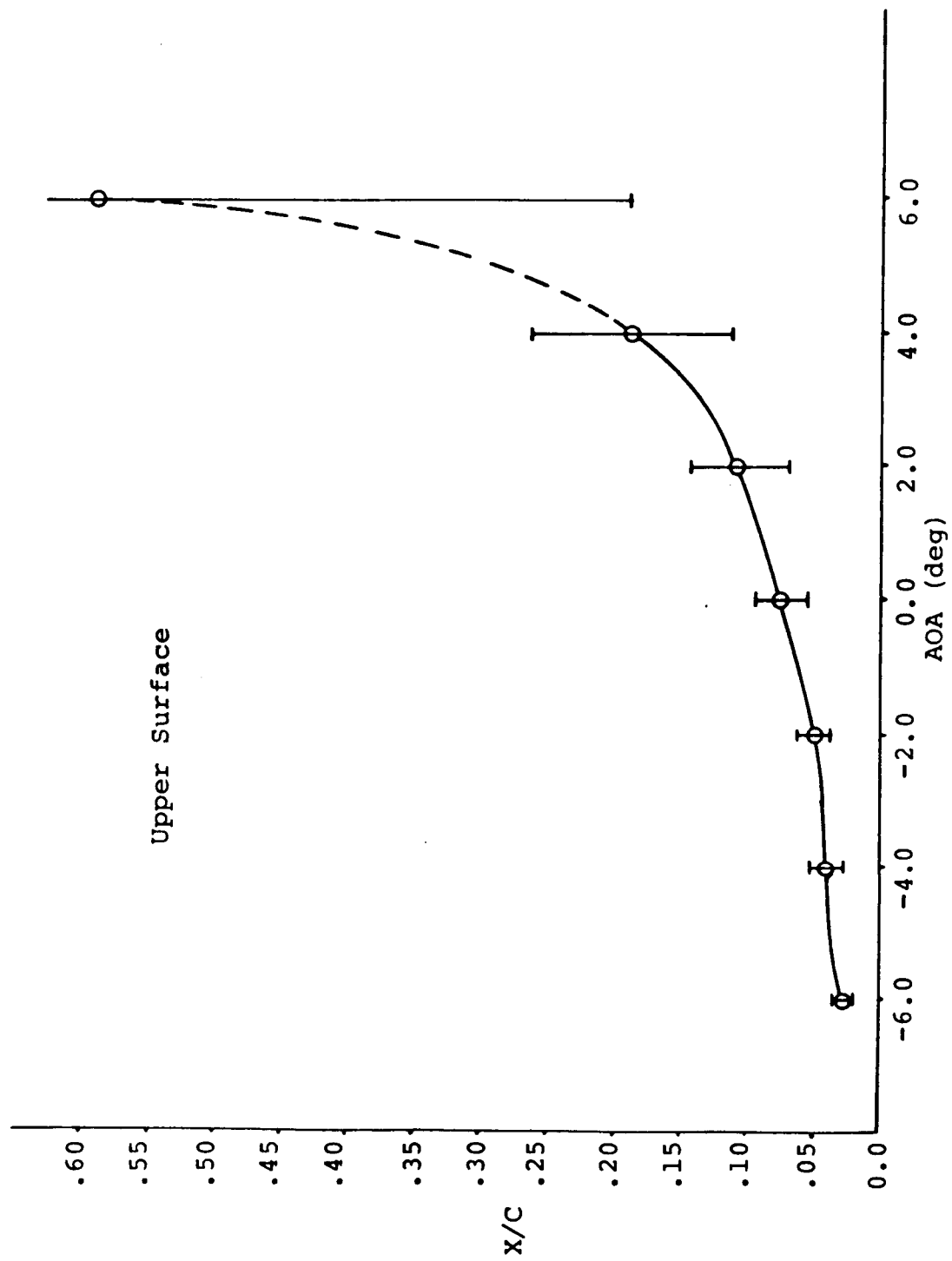


Figure 20. Reattachment Points Reduced from Pressure Plots of Reference 9 for $Re = 1.8 \times 10^6$.

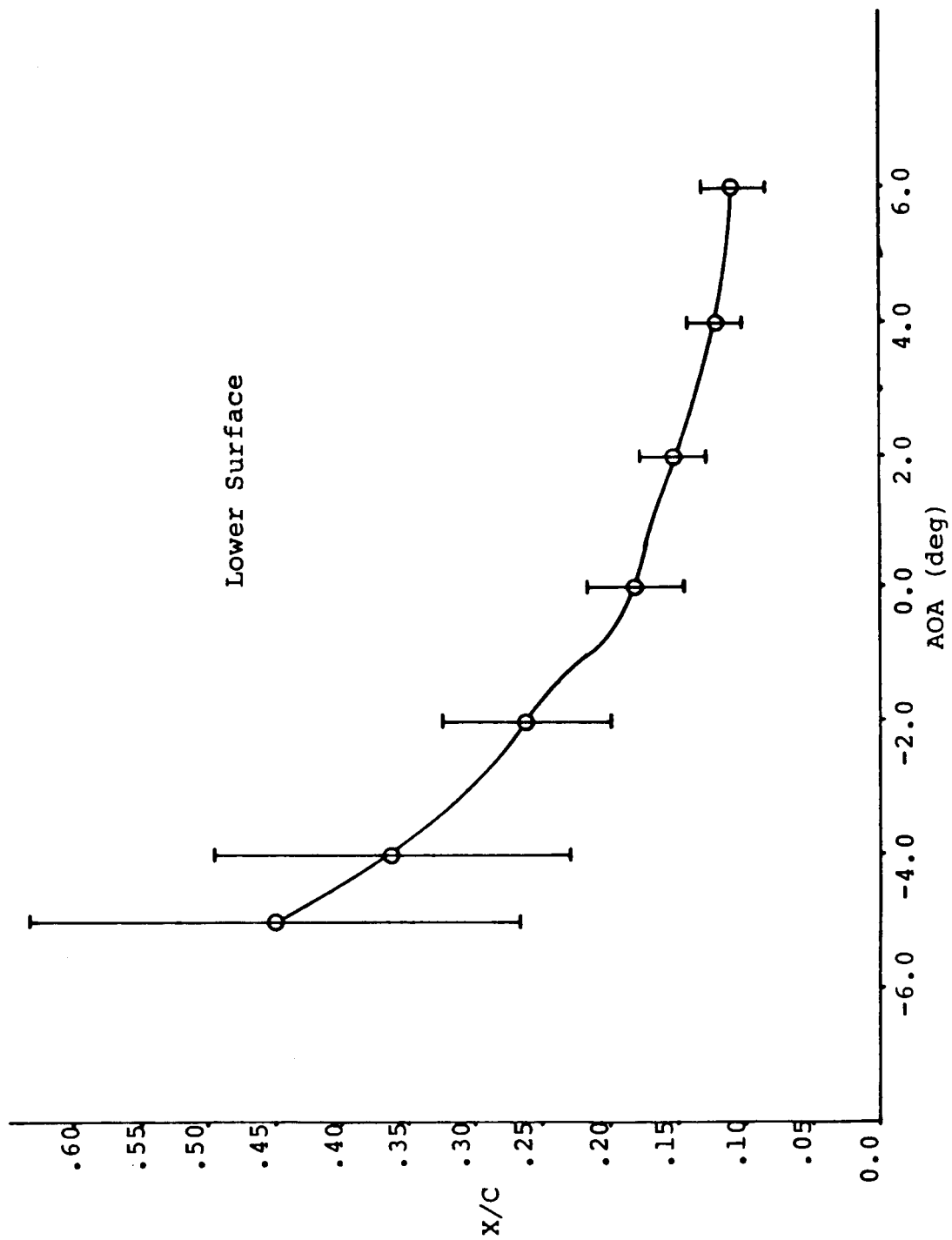


Figure 21. Reattachment Points Reduced From Pressure Plots of Reference 9 for $Re = 0.85 \times 10^6$.

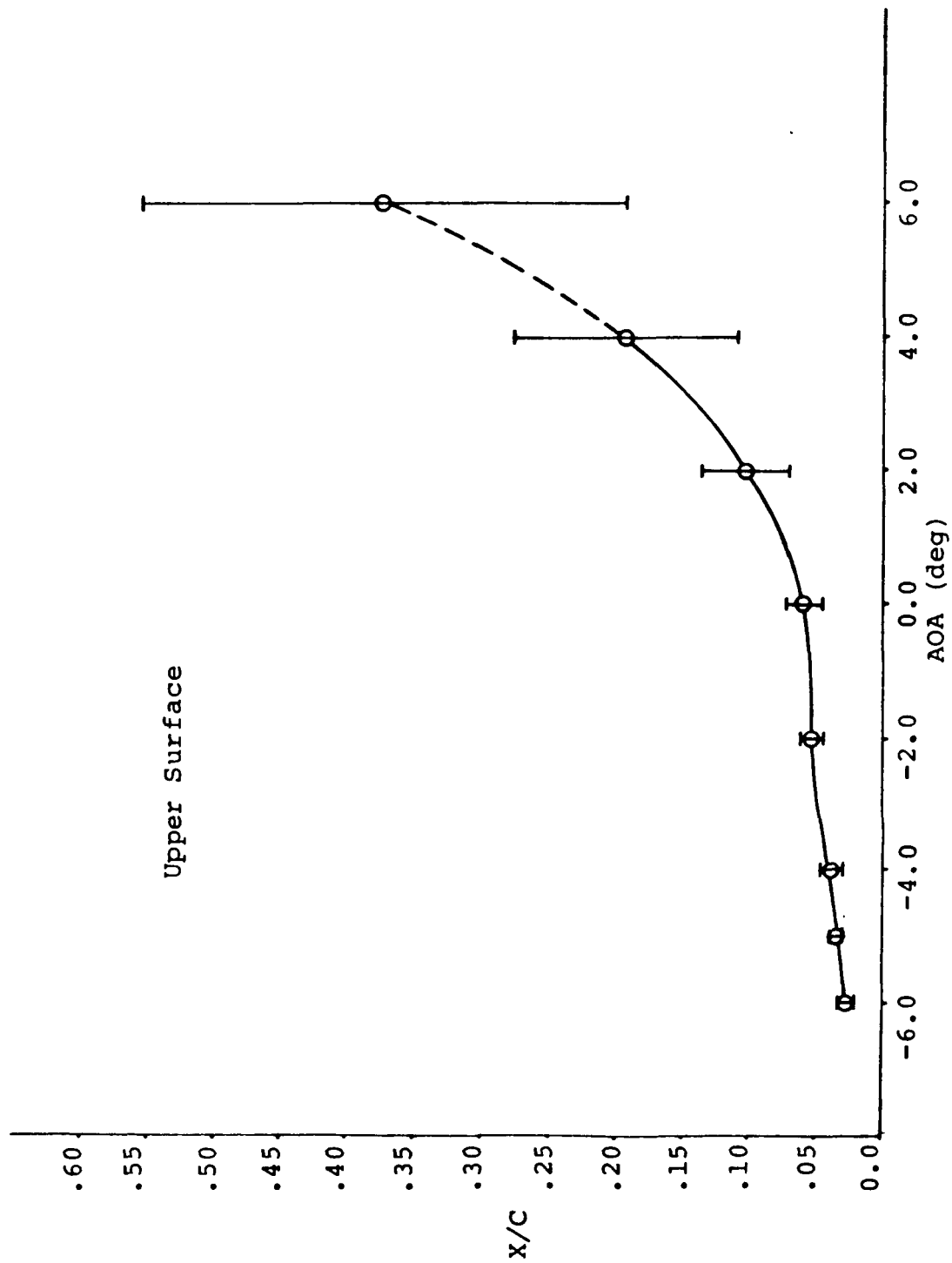


Figure 22. Reattachment Points Reduced from Pressure Plots of Reference 9 for $Re = 0.85 \times 10^6$.

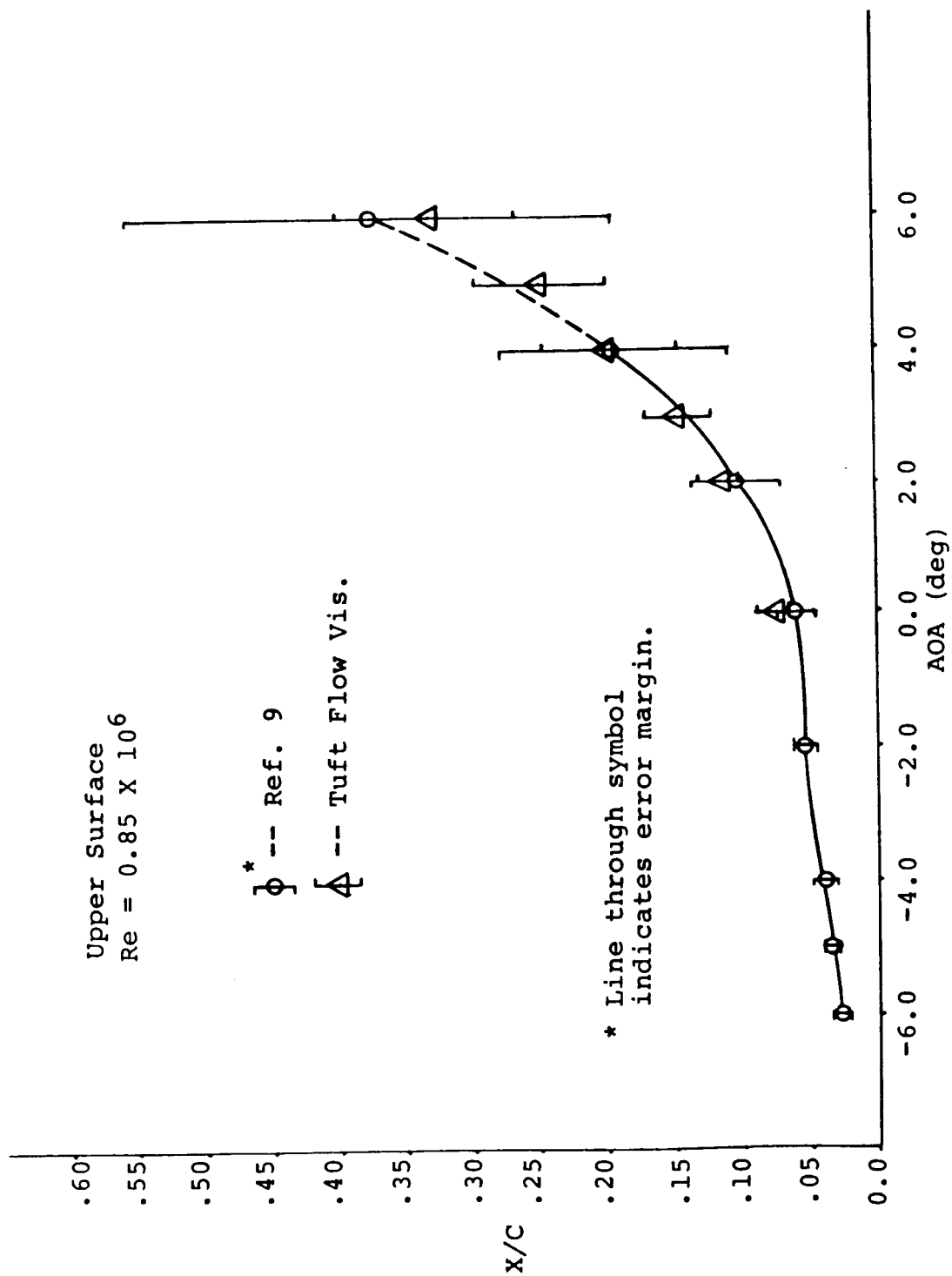


Figure 23. Reattachment Points for Upper Surface Reduced from Tuft Flow Visualization Photographs.

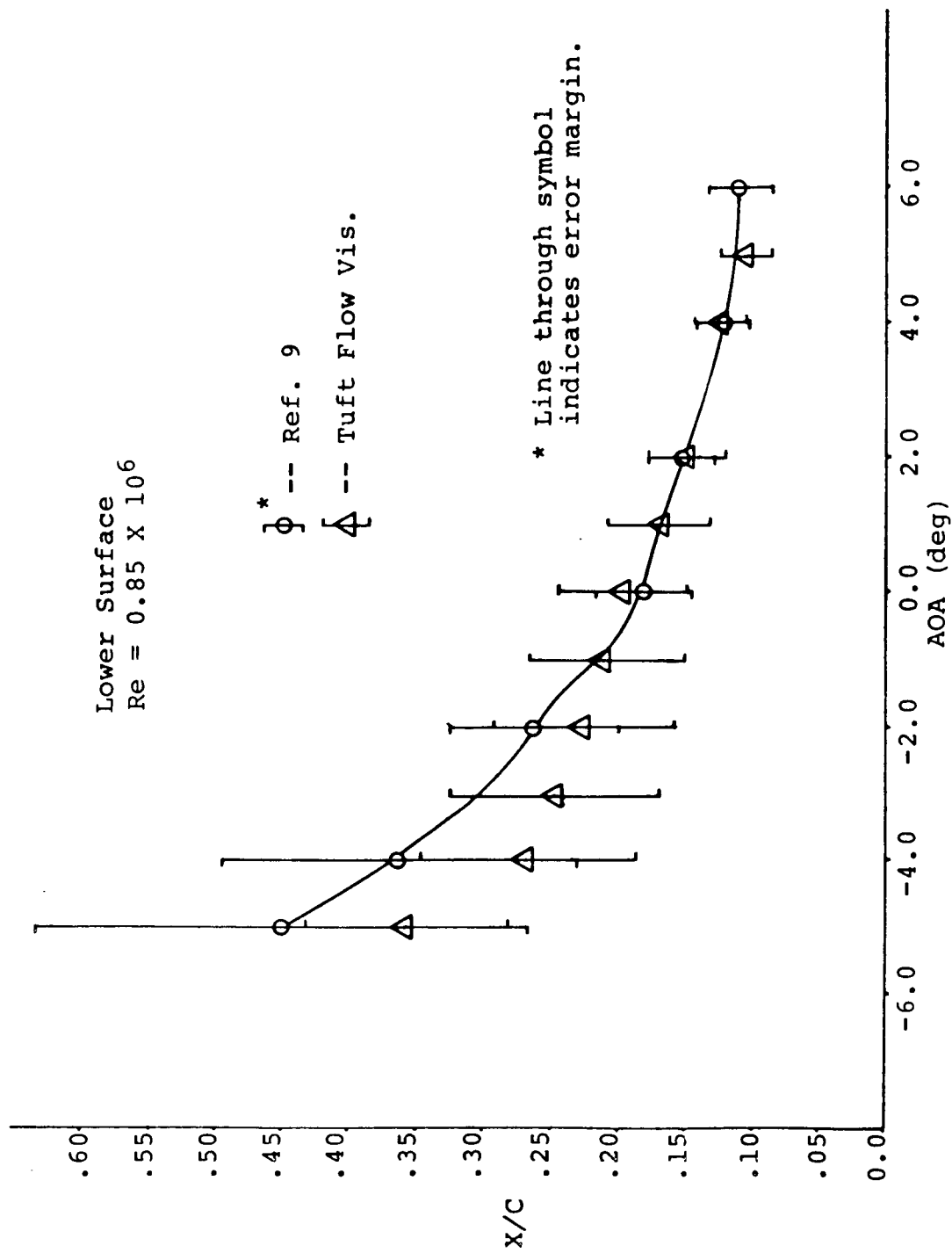


Figure 24. Reattachment Points for Lower Surface Reduced from Tuft Flow Visualization Photographs.

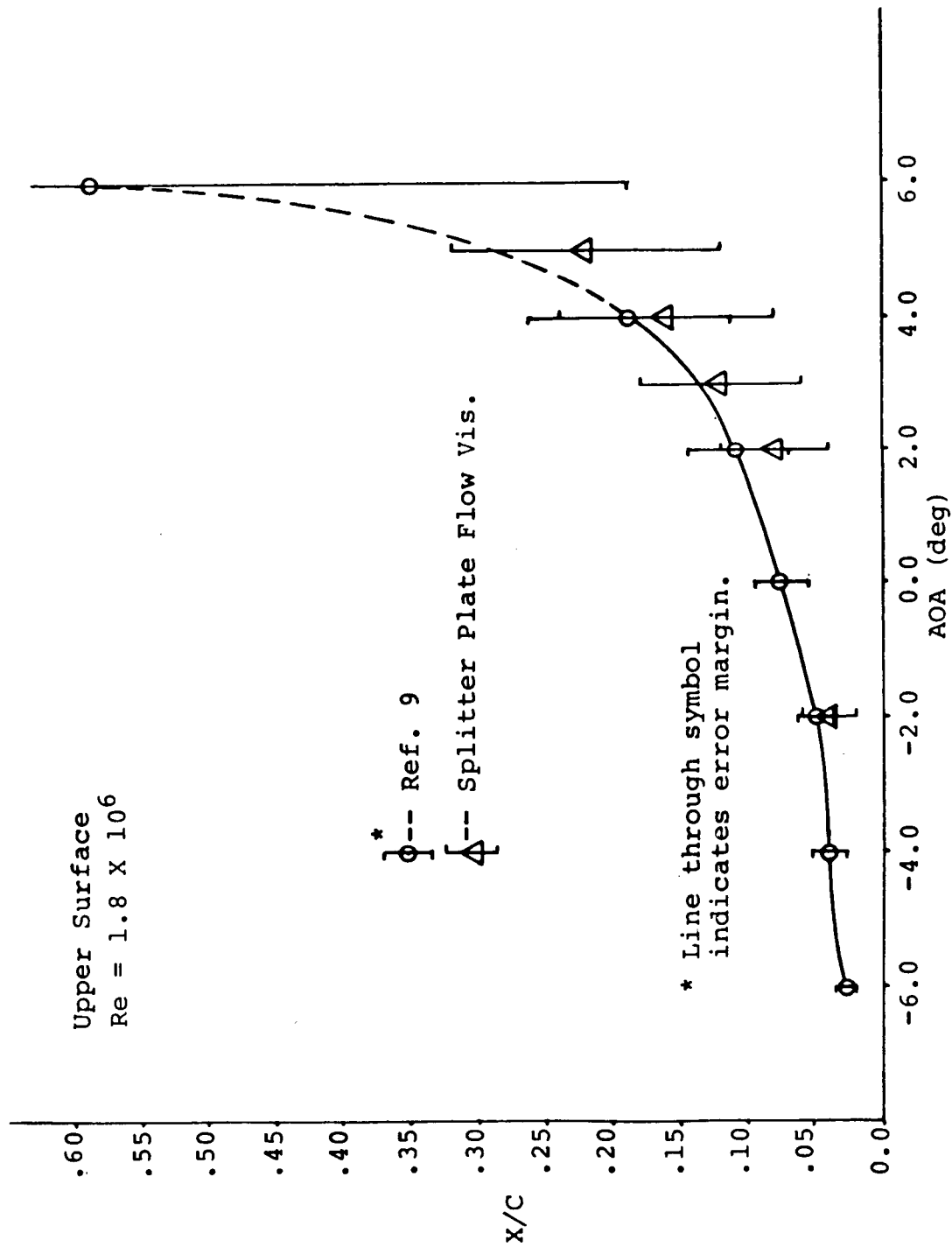


Figure 25. Reattachment Points for Upper Surface Reduced from Splitter Plate Flow Visualization Photographs.

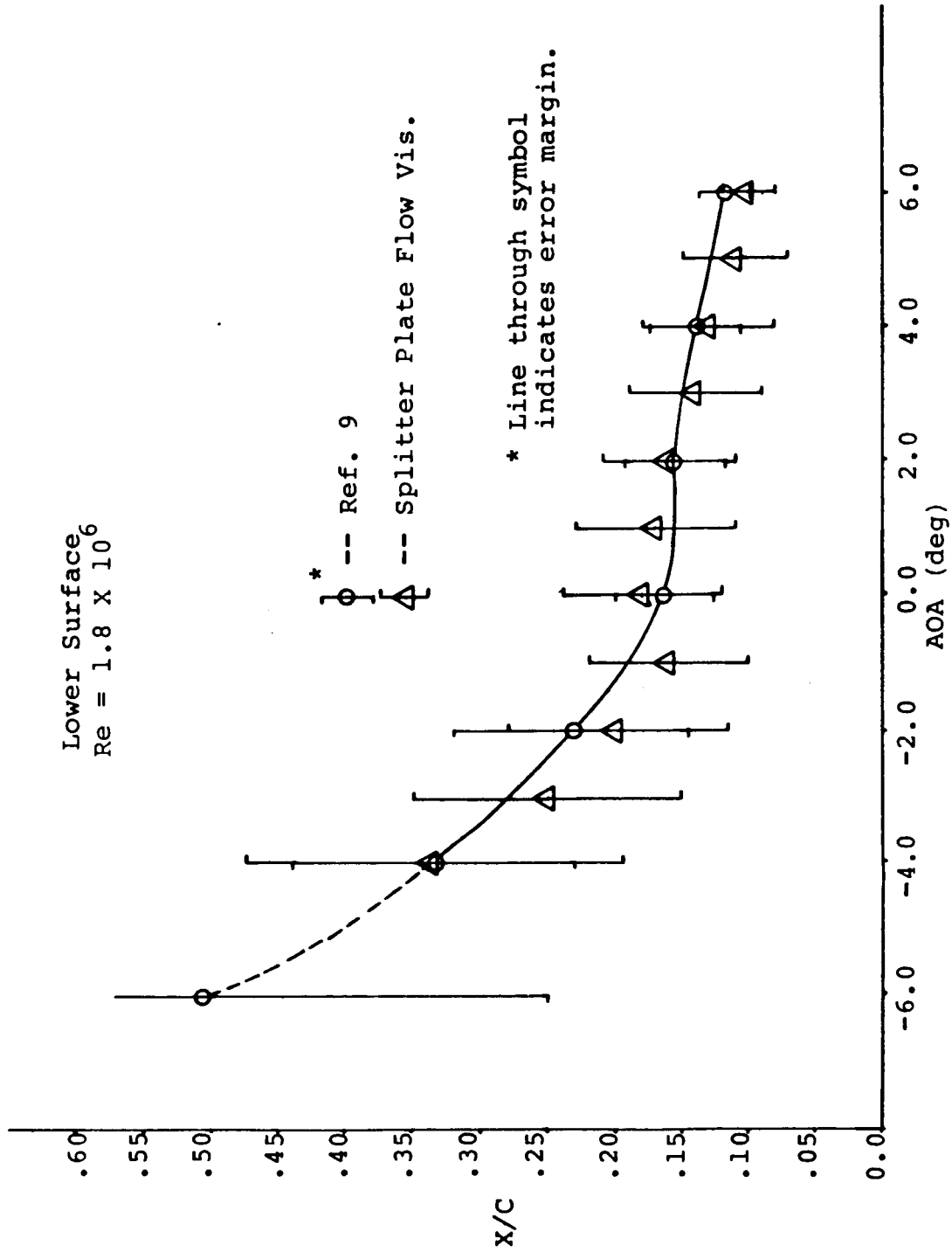


Figure 26. Reattachment Points for Lower Surface Reduced from Splitter Plate Flow Visualization Photographs.

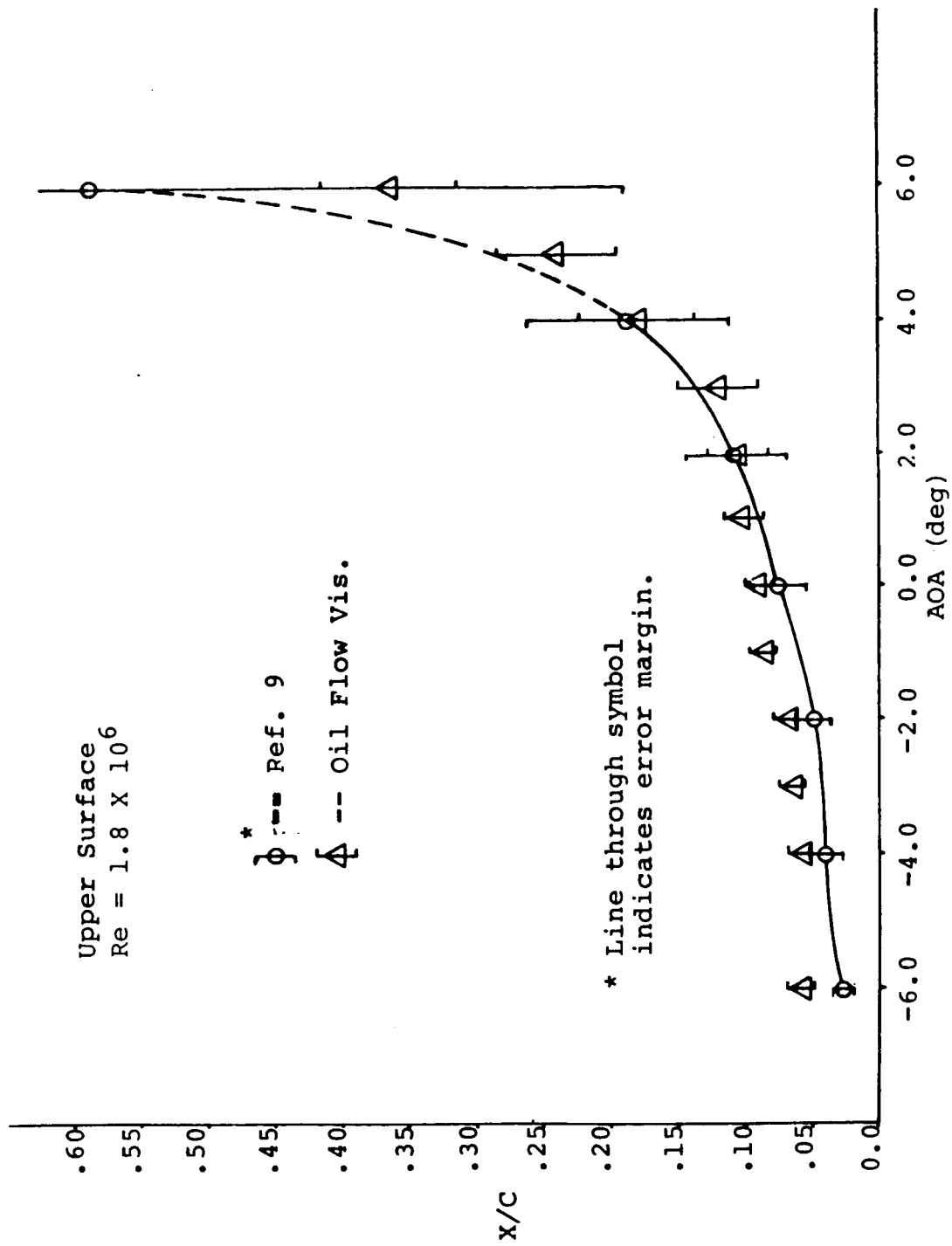


Figure 27. Reattachment Points for Upper Surface Reduced from Oil Flow Visualization Photographs.

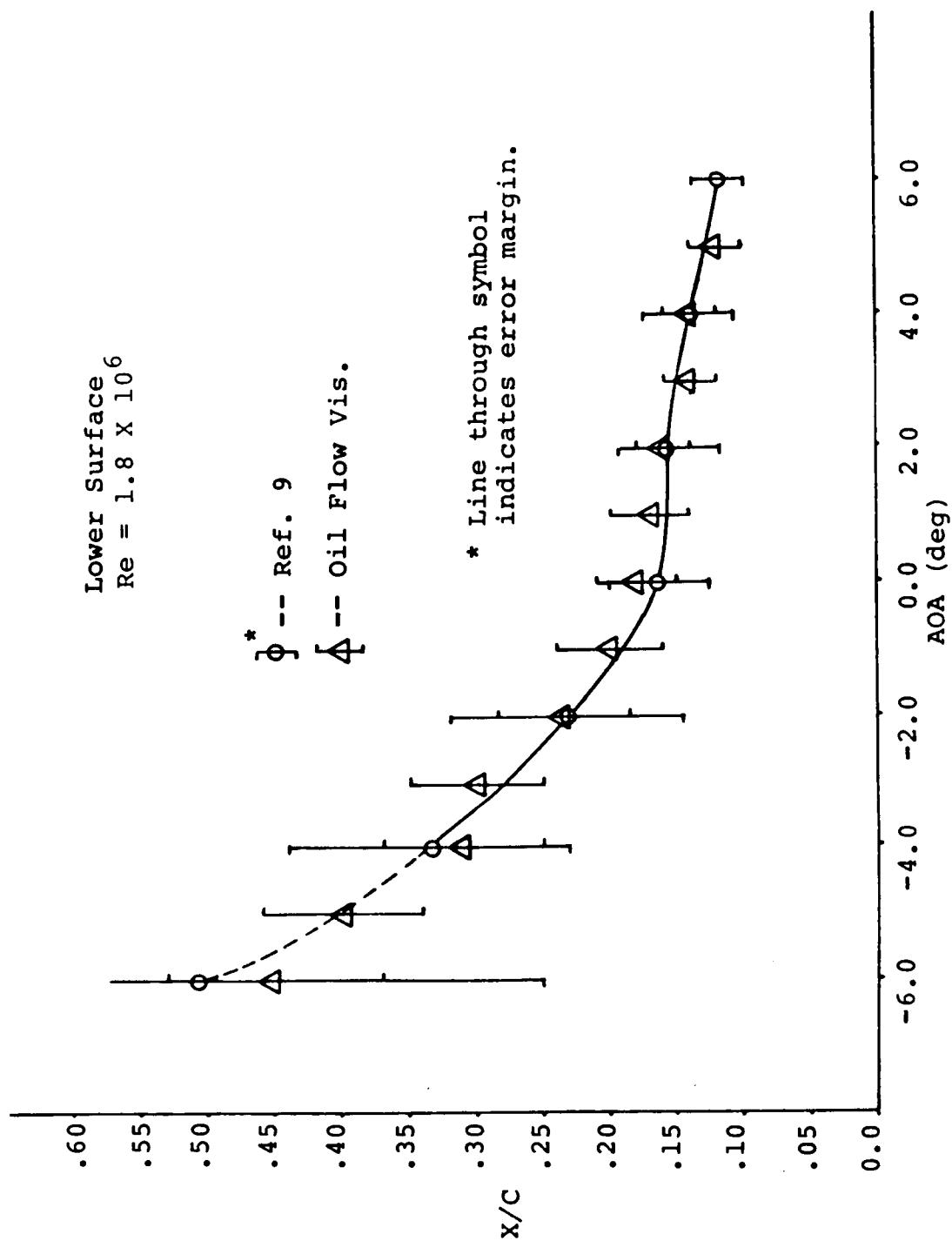
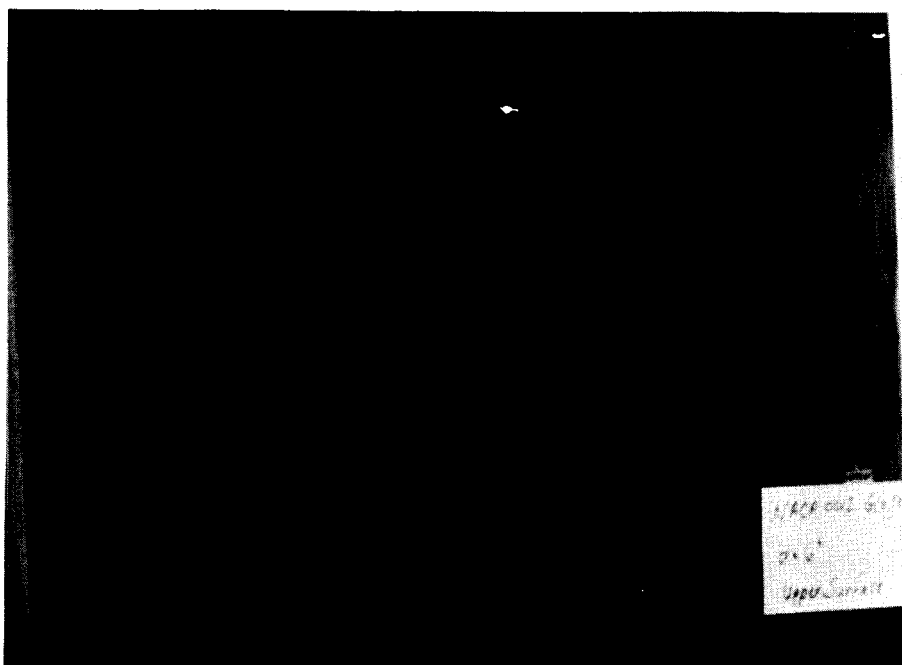
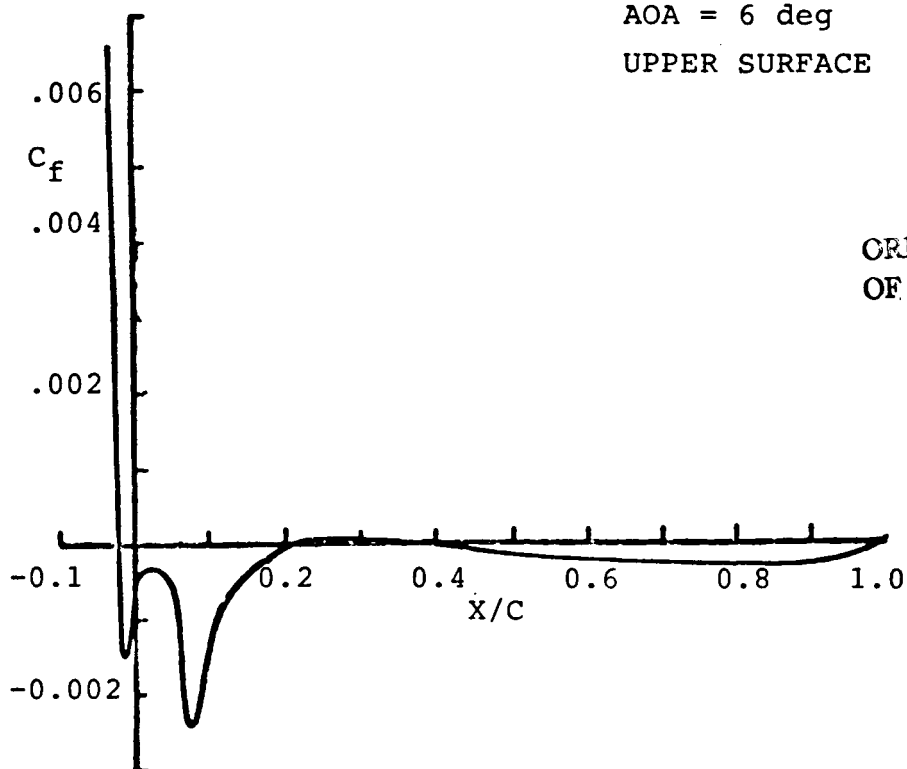


Figure 28. Reattachment Points for Lower Surface Reduced from Oil Flow Visualization Photographs.



$\left\{ \begin{array}{l} 34\% \text{ CHORD} \\ 28\% \text{ CHORD} \end{array} \right.$

AOA = 6 deg
 UPPER SURFACE



ORIGINAL PAGE IS
 OF POOR QUALITY

Figure 29. Comparison of C_f Plot of Reference 17
 with the Oil Flow Pattern for the
 Upper Surface of the NACA 0012.

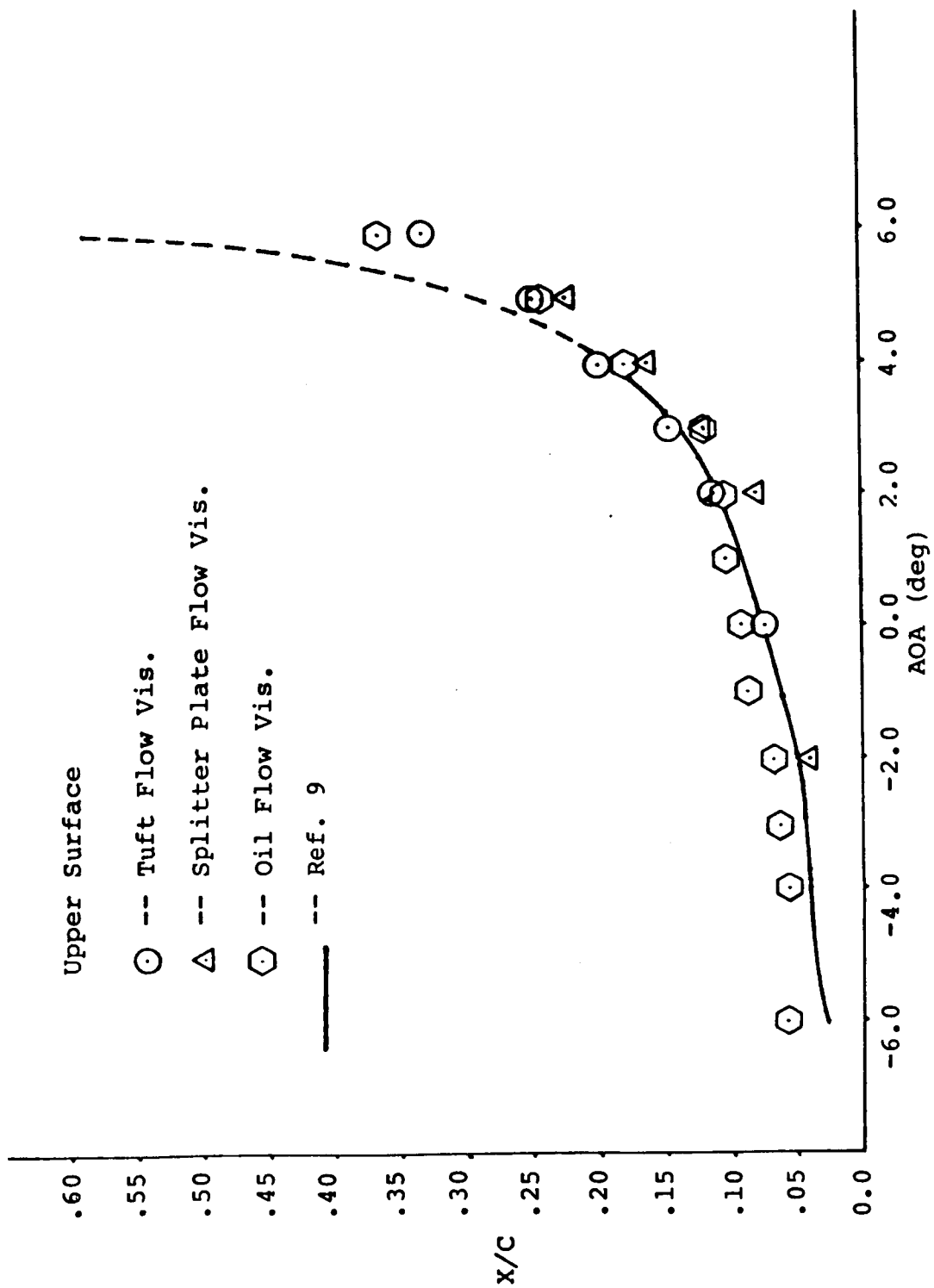


Figure 30. Comparison of Reattachment Points Reduced from Tuft, Oil, and Splitter Plate Flow Visualization Photographs for the Upper Surface.

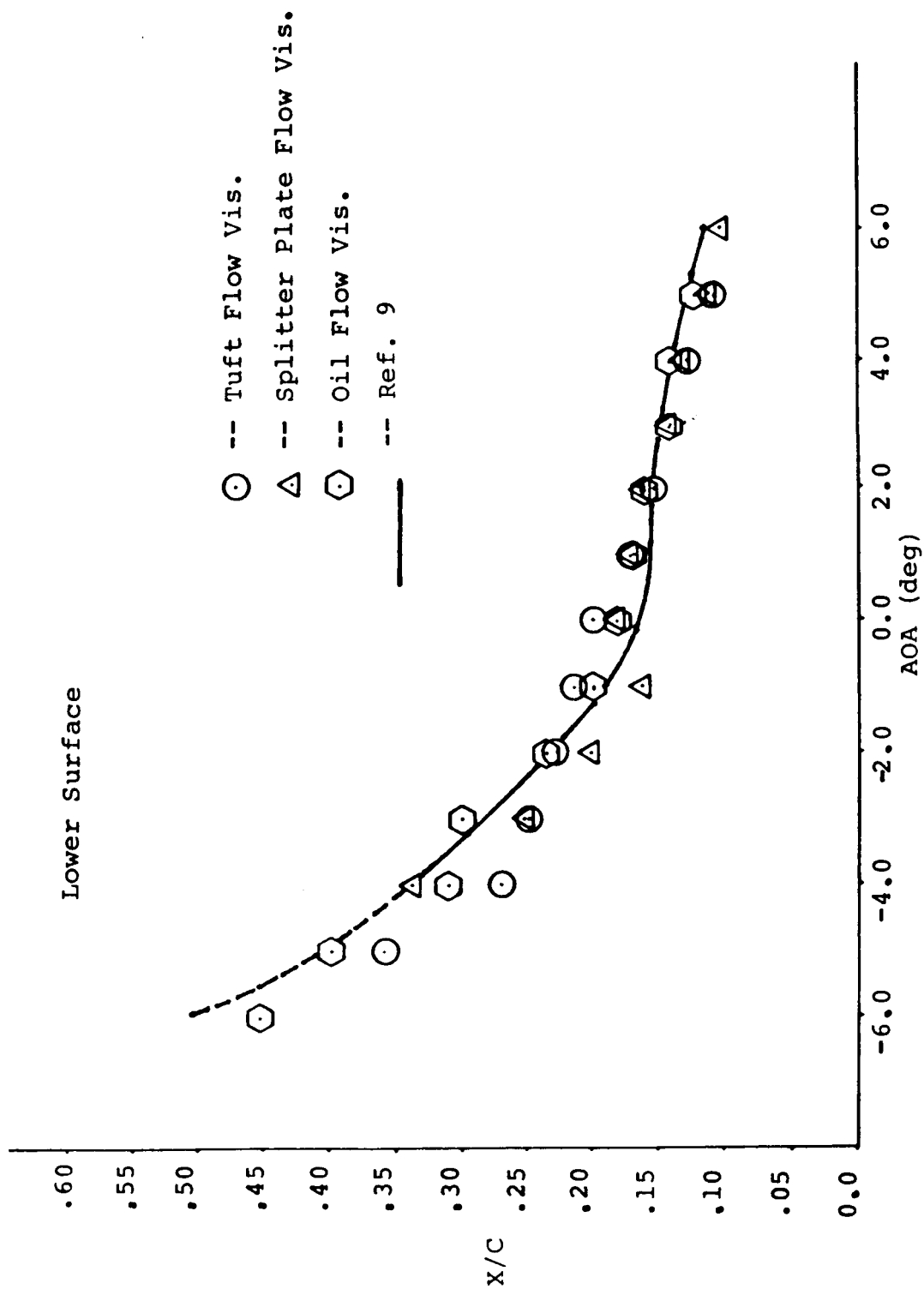


Figure 31 . Comparison of Reattachment Points Reduced from Tuft, Oil, and Splitter Plate Flow Visualization Photographs for the Lower Surface.

TABLE 1. COORDINATES FOR THE NACA 0012 MODEL -
CLEAN CONFIGURATION

No.	X _u	Y _u	X _l	Y _l
1.	0.00000	0.00000	0.00000	0.00000
2.	0.00309	0.00967	0.00309	-0.00967
3.	0.00621	0.01356	0.00621	-0.01356
4.	0.01380	0.01984	0.02230	-0.02481
5.	0.02230	0.02481	0.04080	-0.03256
6.	0.03140	0.02899	0.08000	-0.04307
7.	0.04080	0.03256	0.12000	-0.04988
8.	0.05000	0.03555	0.16000	-0.05442
9.	0.06000	0.03838	0.20000	-0.05738
10.	0.07000	0.04086	0.24000	-0.05913
11.	0.08000	0.04307	0.28000	-0.05993
12.	0.09000	0.04505	0.32000	-0.05993
13.	0.10000	0.04683	0.36000	-0.05926
14.	0.11000	0.04843	0.40000	-0.05803
15.	0.12000	0.04988	0.44000	-0.05631
16.	0.13000	0.05119	0.48000	-0.05294
17.	0.14000	0.05238	0.56000	-0.04878
18.	0.15000	0.05345	0.60000	-0.04563
19.	0.16000	0.05442	0.65000	-0.04132
20.	0.17000	0.05529	0.70000	-0.03664
21.	0.18000	0.05607	0.75000	-0.03160
22.	0.19000	0.05676	0.80000	-0.02623
23.	0.20000	0.05738	0.85000	-0.02053
24.	0.21000	0.05792	0.90000	-0.01448
25.	0.22000	0.05839	0.95000	-0.00807
26.	0.23000	0.05879	0.97500	-0.00471
27.	0.24000	0.05913	1.00000	0.00000
28.	0.25000	0.05941		
29.	0.26000	0.05864		
30.	0.27000	0.05981		
31.	0.28000	0.05993		
32.	0.29000	0.06000		
33.	0.30000	0.06002		
34.	0.31000	0.05999		
35.	0.32000	0.05993		
36.	0.33000	0.05982		
37.	0.34000	0.05967		
38.	0.35000	0.05949		
39.	0.36000	0.05926		
40.	0.37000	0.05900		
41.	0.38000	0.05871		
42.	0.39000	0.05839		
43.	0.40000	0.05803		
44.	0.42000	0.05723		
45.	0.44000	0.05631		

TABLE 1. CONTINUED

No.	X u	Y u
46.	0.47000	0.05473
47.	0.50000	0.05294
48.	0.53000	0.05095
49.	0.56000	0.04878
50.	0.60000	0.04563
51.	0.65000	0.04132
52.	0.70000	0.03664
53.	0.75000	0.03160
54.	0.80000	0.02623
55.	0.85000	0.02053
56.	0.90000	0.01448
57.	0.95000	0.00807
58.	0.97500	0.00471
59.	1.00000	0.00000

TABLE 2. COORDINATES FOR THE NACA 0012 MODEL -
GLAZE ICE CONFIGURATION

No.	X u	Y u	X l	Y l
1.	-0.02660	0.01690*	-0.02660	0.01690
2.	-0.02450	0.02870*	-0.02220	0.00390
3.	-0.02080	0.03060*	-0.01750	-0.00700
4.	-0.01000	0.02880	-0.01070	-0.01840
5.	-0.00010	0.02680	-0.00360	-0.02840
6.	0.01000	0.02500	0.00590	-0.03930
7.	0.02210	0.02670	0.01500	-0.04740
8.	0.03110	0.03000	0.02580	-0.05330**
9.	0.04070	0.03330	0.03000	-0.05300**
10.	0.04910	0.03610	0.03970	-0.05030
11.	0.05950	0.03900	0.04950	-0.04730
12.	0.06940	0.04140	0.06000	-0.04410
13.	0.07940	0.04350	0.06950	-0.04210
14.	0.08910	0.04550	0.07930	-0.04360
15.	0.09900	0.04720	0.10940	-0.04870
16.	0.10970	0.04870	0.11930	-0.05000
17.	0.11970	0.05000	0.12900	-0.05110
18.	0.12969	0.05140	0.14000	-0.05200
19.	0.14000	0.05240	0.16000	-0.05442
20.	0.16000	0.05442	0.20000	-0.05738
21.	0.17000	0.05500	0.24000	-0.05913
22.	0.18000	0.05607	0.28000	-0.05993
23.	0.19000	0.05676	0.32000	-0.05993
24.	0.20000	0.05738	0.36000	-0.05926
25.	0.21000	0.05792	0.40000	-0.05803
26.	0.22000	0.05839	0.44000	-0.05631
27.	0.23000	0.05879	0.50000	-0.05294
28.	0.24000	0.05913	0.56000	-0.04878
29.	0.25000	0.05941	0.60000	-0.04563
30.	0.26000	0.05864	0.70000	-0.03664
31.	0.28000	0.05993	0.75000	-0.03160
32.	0.30000	0.06002	0.85000	-0.02053
33.	0.32000	0.05993	0.90000	-0.01448
34.	0.34000	0.05967	0.95000	-0.00807
35.	0.36000	0.05926	0.97500	-0.00471
36.	0.38000	0.05871	1.00000	0.00000
37.	0.40000	0.05800		
38.	0.42000	0.05700		
39.	0.44000	0.05631		
40.	0.47000	0.05473		
41.	0.50000	0.05294		
42.	0.53000	0.05095		
43.	0.56000	0.04878		
44.	0.60000	0.04563		
45.	0.70000	0.03664		

TABLE 2. CONTINUED

No.	X	Y
	u	u
46.	0.75000	0.03160
47.	0.80000	0.02623
48.	0.85000	0.02053
49.	0.90000	0.01448
50.	0.95000	0.00807
51.	0.97500	0.00471
52.	1.00000	0.00000

* NOTE: Upper surface horn radius of
curvature, $(r/c)_u = 0.002232$.

** NOTE: Lower surface horn radius of
curvature, $(r/c)_l = 0.01042$.

TABLE 3. PHYSICAL PROPERTIES OF HYDROCARBONS
 USED FOR SMOKE GENERATION
 (Adapted from reference 21)

	Boiling Point F, (C)	Flash Point F, (C)	Auto Ignition F, (C)
Mineral Oil	600 (315.5)	275 - 500 (135 - 260)	500 - 700 (260 - 371)
Kerosene	350 - 550 (176.6 - 287.7)	110 - 130 (43.3 - 54.4)	440 - 560 (226.6 - 293.3)
Coal Tar	96 (35.5)	60 - 77 (15.5 - 25)	-

TABLE 4. REATTACHMENT POINTS FOR UPPER AND LOWER SURFACES
OF THE NACA 0012 AIRFOIL WITH GLAZE ICE.
(From Tuft Flow Visualization, $Re = 0.85 \times 10^6$)

a) Upper surface

AOA (deg)	X/C
=====	
0	0.073
2	0.115
3	0.142
4	0.197
5	0.247
6	0.330

b) Lower surface

AOA (deg)	X/C
=====	
0	0.196
1	0.169
2	0.150
4	0.125
5	0.104
-1	0.213
-2	0.226
-3	0.247
-4	0.267
-5	0.359

TABLE 5. REATTACHMENT POINTS FOR UPPER AND LOWER SURFACES
OF THE NACA 0012 AIRFOIL WITH GLAZE ICE.
(From Splitter Plate Studies, $Re = 1.79 \times 10^6$)

a) Upper Surface

AOA (deg)	X/C
=====	
0	-
1	0.065
2	0.080
3	0.120
4	0.160
5	0.220
6	-
-1	-
-2	0.040
-3	-
-4	-
-5	-

b) Lower Surface

AOA (deg)	X/C
=====	
0	0.180
1	0.170
2	0.160
3	0.140
4	0.130
5	0.110
6	0.100
-1	0.160
-2	0.200
-3	0.250
-4	0.340
-5	-

TABLE 6. REATTACHMENT POINTS FOR UPPER AND LOWER SURFACES
OF THE NACA 0012 AIRFOIL WITH GLAZE ICE.
(From Surface Oil Flow Visualization,
 $Re = 1.77 \times 10^6$)

a) Upper Surface

AOA (deg)	X/C
=====	
0	0.084
1	0.102
2	0.106
3	0.120
4	0.180
5	0.241
6	0.364
-1	0.089
-2	0.070
-3	0.065
-4	0.060
-5	0.067
-6	0.057

b) Lower Surface

AOA (deg)	X/C
=====	
0	0.180
1	0.170
2	0.160
3	0.140
4	0.140
5	0.120
-1	0.200
-2	0.235
-3	0.300
-4	0.310
-5	0.400
-6	0.450

TABLE 7. REATTACHMENT POINT FOR UPPER AND LOWER SURFACES
OF THE NACA 0012 AIRFOIL WITH GLAZE ICE.

a) From Reference 25, $Re = 1.40 \times 10^6$

AOA (deg)	X/C upper	X/C lower
0	0.071 (0.010)*	0.179 (0.020)
2	0.092 (0.010)	0.150 (0.010)
4	0.171 (0.010)	0.131 (0.010)

b) From Reference 9, $Re = 1.40 \times 10^6$

AOA (deg)	X/C upper	X/C lower
0	0.072 (0.019)	0.183 (0.052)
2	0.108 (0.031)	0.159 (0.038)
4	0.186 (0.084)	0.144 (0.036)

* Number in parenthesis is the error margin.

TABLE 8. REATTACHMENT POINTS FOR UPPER AND LOWER
SURFACES OF THE NACA 0012 WITH GLAZE ICE
(From Reference 9)

a) $Re = 1.85 \times 10^6$

AOA (deg)	X/C upper	X/C lower
0	0.075 (0.019) *	0.163 (0.031)
2	0.109 (0.038)	0.156 (0.038)
4	0.188 (0.075)	0.138 (0.034)
6	0.590 (0.406)	0.116 (0.019)
-2	0.047 (0.013)	0.231 (0.088)
-4	0.040 (0.013)	0.334 (0.103)
-6	0.028 (0.006)	0.506 (0.256)

b) $Re = 0.84 \times 10^6$

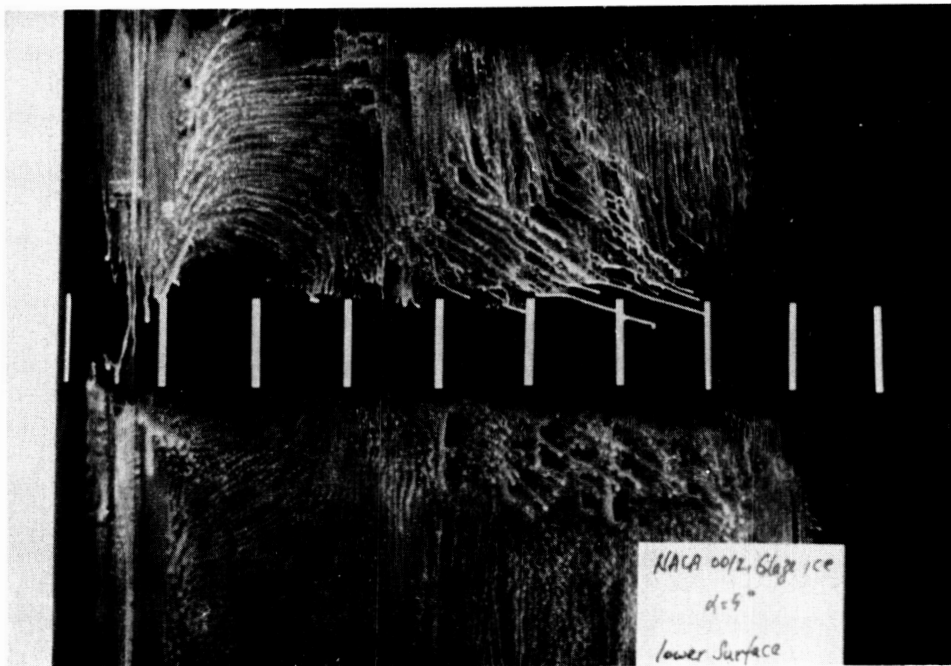
AOA (deg)	X/C upper	X/C lower
0	0.059 (0.013)	0.181 (0.034)
2	0.109 (0.033)	0.153 (0.022)
4	0.194 (0.084)	0.122 (0.016)
6	0.375 (0.181)	0.113 (0.025)
-2	0.053 (0.009)	0.263 (0.063)
-4	0.033 (0.008)	0.363 (0.131)
-5	0.035 (0.005)	0.450 (0.181)
-6	0.028 (0.006)	-

* Number in parenthesis is the error margin.

APPENDIX

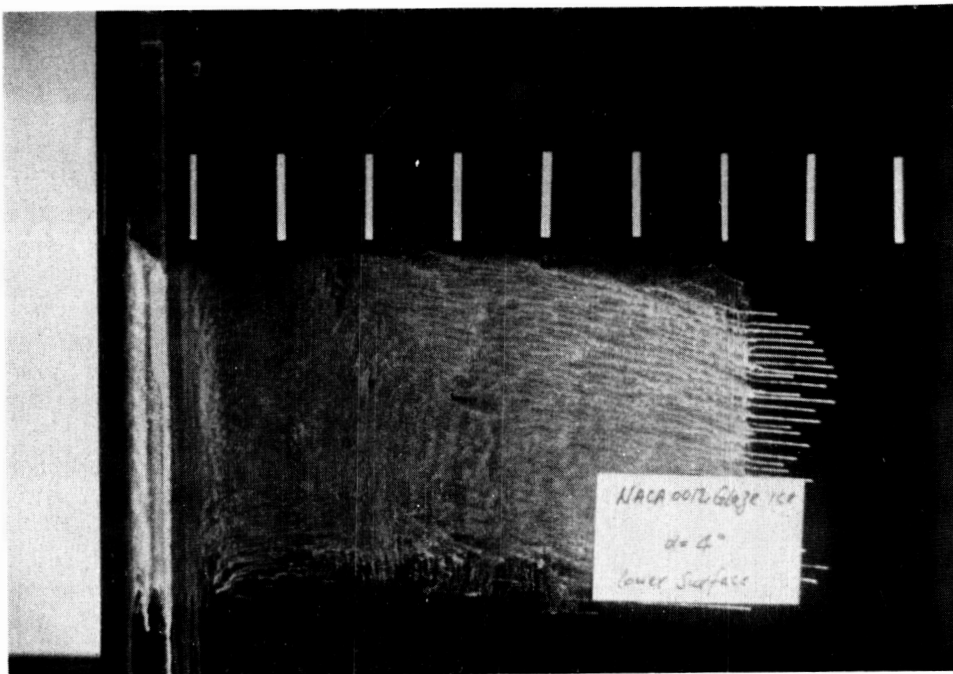
AN ALBUM OF LEADING EDGE SEPARATION BUBBLE GROWTH
ON A NACA 0012 AIRFOIL WITH SIMULATED GLAZE ICE
VISUALIZED USING THE SURFACE OIL FLOW TECHNIQUE
FROM -5 TO +4 DEGREES IN ONE DEGREE INCREMENTS

ORIGINAL PAGE IS
OF POOR QUALITY



ERROR BOUND \longrightarrow \longleftarrow
40% CHORD \longrightarrow \longleftarrow

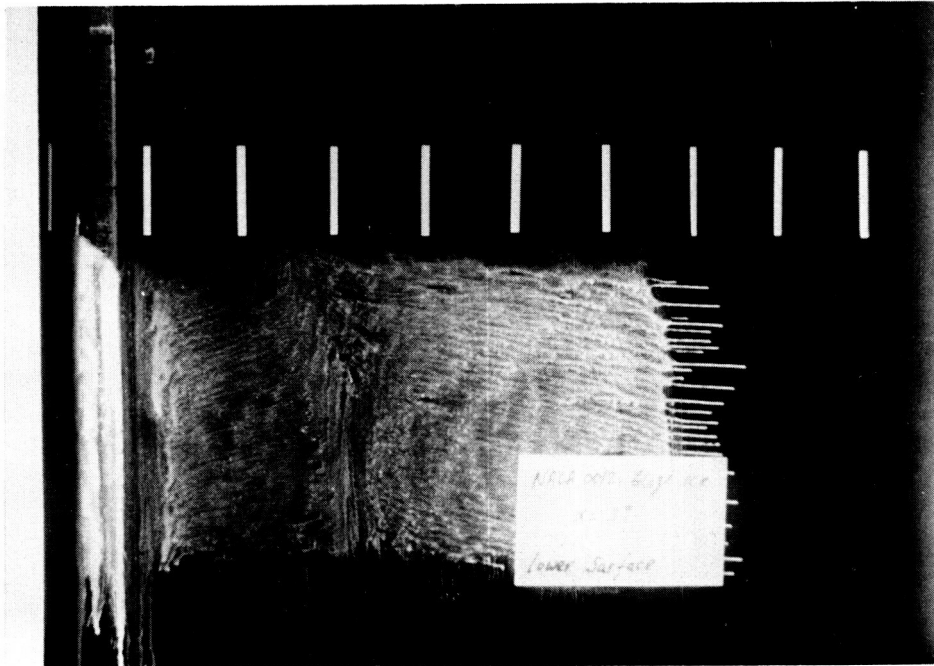
$V = 180$ fps
AOA = -5 deg, LOWER SURFACE



ERROR BOUND \longrightarrow \longleftarrow
31% CHORD \longrightarrow \longleftarrow

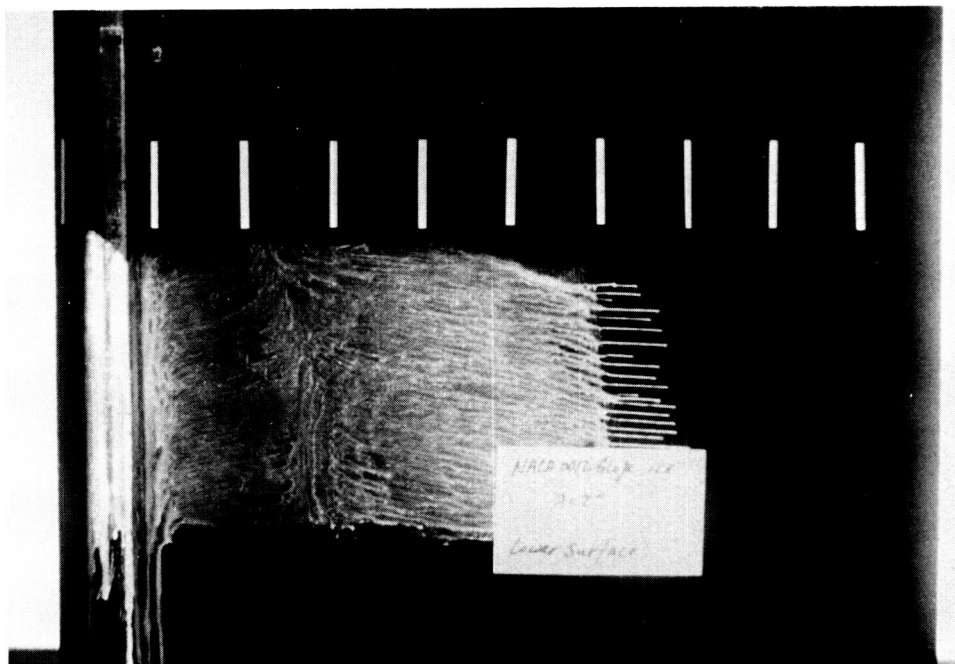
$V = 180$ fps
AOA = -4 deg, LOWER SURFACE

ORIGINAL PAGE IS
OF POOR QUALITY



ERROR BOUND \rightarrow \leftarrow
30% CHORD \rightarrow \leftarrow

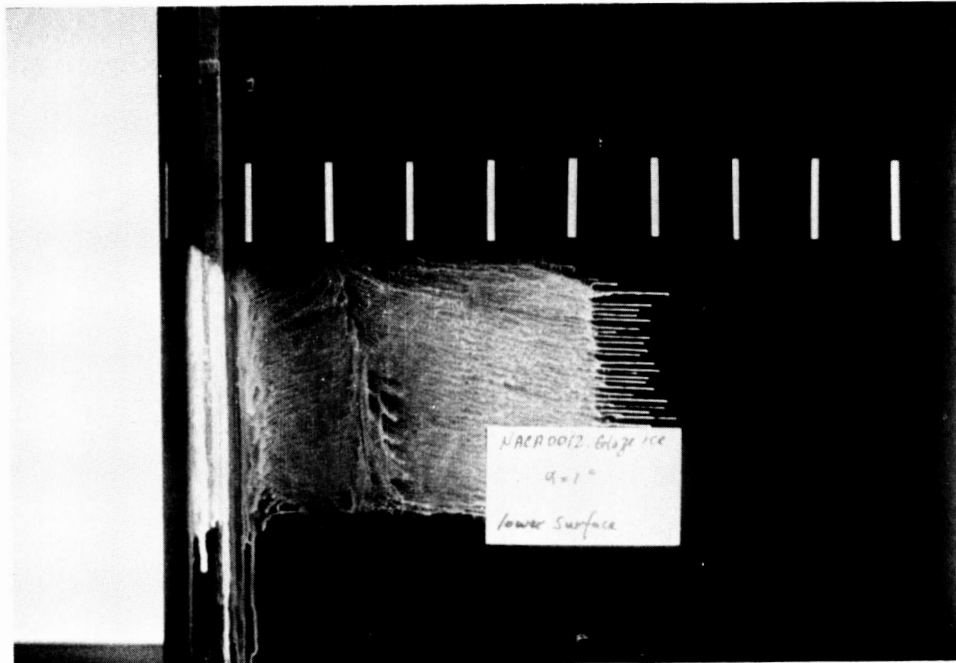
$V = 180$ fps
AOA = -3 deg, LOWER SURFACE

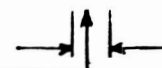


ERROR BOUND \rightarrow \leftarrow
24% CHORD \rightarrow \leftarrow

$V = 180$ fps
AOA = -2 deg, LOWER SURFACE

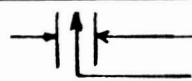
ORIGINAL PAGE IS
OF POOR QUALITY



ERROR BOUND 
20% CHORD

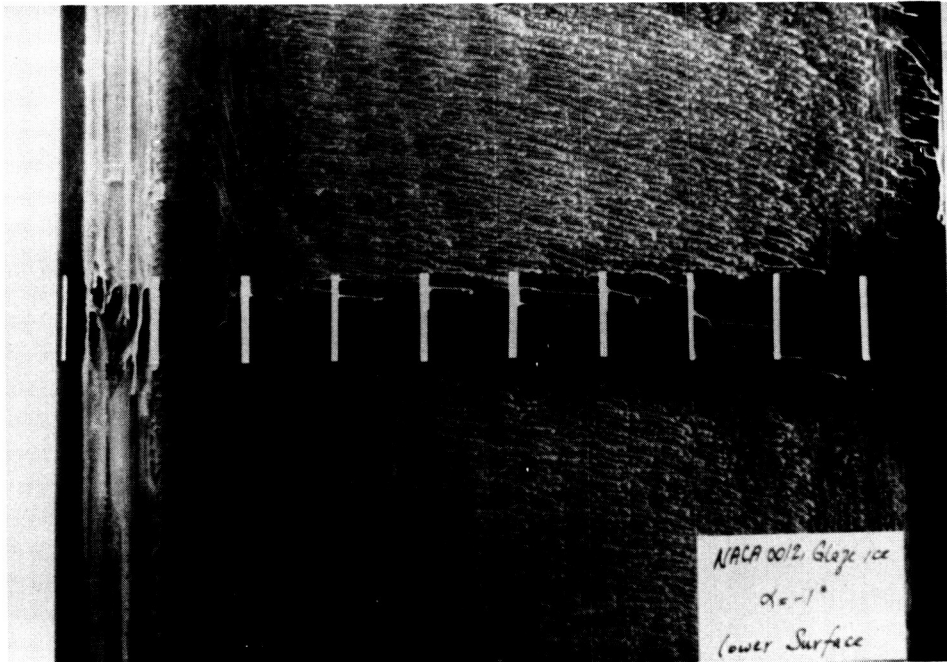
$V = 180 \text{ fps}$
 $\text{AOA} = -1 \text{ deg, LOWER SURFACE}$



 ERROR BOUND
18% CHORD

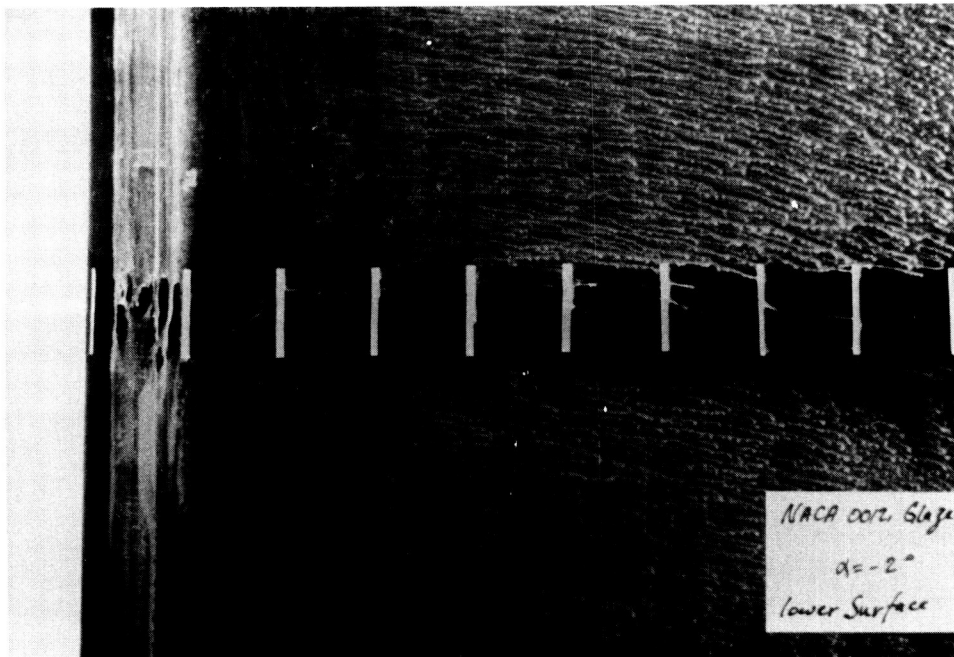
$V = 180 \text{ fps}$
 $\text{AOA} = 0 \text{ deg, LOWER SURFACE}$

ORIGINAL PAGE IS
OF POOR QUALITY



→ | ↑ | ←
ERROR BOUND
17% CHORD

V = 180 fps
AOA = 1 deg, LOWER SURF.

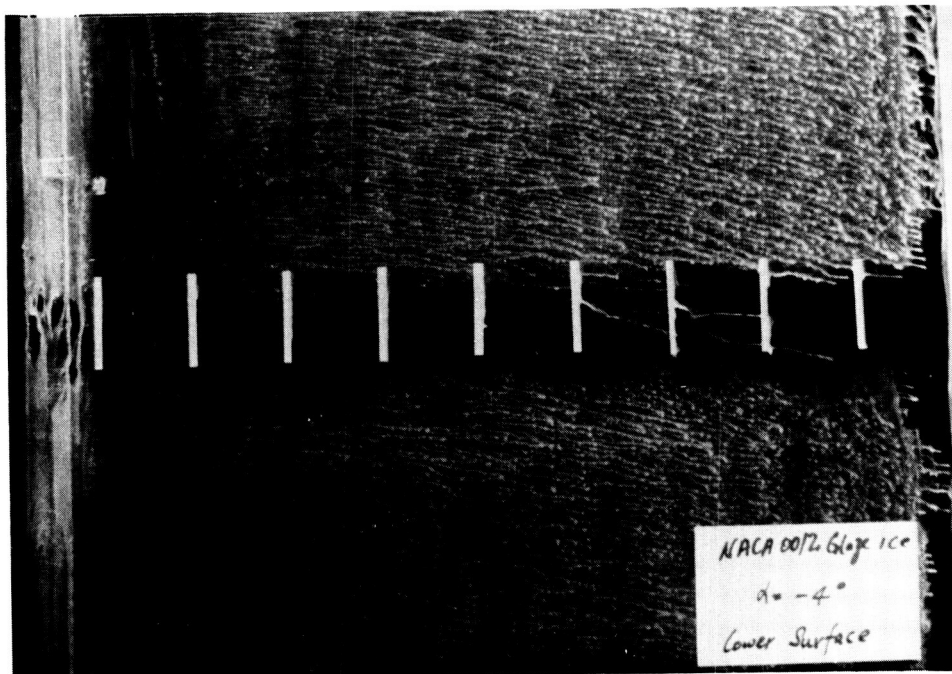


→ | ↑ | ←
ERROR BOUND
16% CHORD

V = 180 fps
AOA = 2 deg, LOWER SURF.

NACA 0012, Glaze ice
 $\alpha = -3^\circ$
 Lower Surface

$\bar{V} = 180 \text{ fps}$
AOA = 3 deg, LOWER SURFACE



V = 180 fps
AOA = 4 deg, LOWER SURFACE

Report Documentation Page

1. Report No. NASA CR-180846		2. Government Accession No.		3. Recipient's Catalog No.	
4. Title and Subtitle A Flow Visualization Study of the Leading Edge Separation Bubble on a NACA 0012 Airfoil With Simulated Glaze Ice				5. Report Date January 1988	
				6. Performing Organization Code NAG3-28	
7. Author(s) Abdollah Khodadoust				8. Performing Organization Report No. None	
				10. Work Unit No. 505-68-11	
9. Performing Organization Name and Address The Ohio State University Dept. of Aeronautical and Astronautical Engineering Columbus, Ohio 43201				11. Contract or Grant No.	
				13. Type of Report and Period Covered Contractor Report Final	
12. Sponsoring Agency Name and Address National Aeronautics and Space Administration Lewis Research Center Cleveland, Ohio 44135-3191				14. Sponsoring Agency Code	
15. Supplementary Notes Project Manager, Robert J. Shaw, Propulsion Systems Division, NASA Lewis Research Center. This report was a thesis submitted in partial fulfillment of the requirements for the degree Master of Science to The Ohio State University.					
16. Abstract As a part of an ongoing research in aircraft icing, the leading edge separation bubble on a NACA 0012 model with a 5 min simulated glaze ice was investigated. The flow visualization methods using oil, tuft, splitter plate, smoke, and liquid crystals were employed to get reattachment line data for the leading edge separation bubble on both surfaces of the airfoil. On the upper surface, the separation bubble was found to grow larger with increasing angles of attack and reduce in size with decreasing angle of attack. On the lower surface, the bubble was found to grow larger with increasing negative angles of attack and reduce in size with increasing angles of attack. The separated flow fails to reattach beyond 6° for the upper surface and -5° for the lower surface. The results of this study compared well with those of other experiments and computational results.					
17. Key Words (Suggested by Author(s)) Aircraft icing Iced airfoil flowfield measurements Computer code validation data				18. Distribution Statement Unclassified - Unlimited Subject Category 02	
19. Security Classif. (of this report) Unclassified		20. Security Classif. (of this page) Unclassified		21. No of pages 90	
				22. Price* A05	